Ultrasound Matrix Imaging. II. The distortion matrix for aberration correction over multiple isoplanatic patches.

William Lambert, Laura A. Cobus, Mathias Fink, Alexandre Aubry

▶ **To cite this version:**

William Lambert, Laura A. Cobus, Mathias Fink, Alexandre Aubry. Ultrasound Matrix Imaging. II. The distortion matrix for aberration correction over multiple isoplanatic patches.. 2021. hal-03158858v1

HAL Id: hal-03158858

https://hal.science/hal-03158858v1

Preprint submitted on 4 Mar 2021 (v1), last revised 3 Dec 2022 (v3)

HAL is a multi-disciplinary open access archive for the deposit and dissemination of scientific research documents, whether they are published or not. The documents may come from teaching and research institutions in France or abroad, or from public or private research centers.

L'archive ouverte pluridisciplinaire **HAL**, est destinée au dépôt et à la diffusion de documents scientifiques de niveau recherche, publiés ou non, émanant des établissements d'enseignement et de recherche français ou étrangers, des laboratoires publics ou privés.

Ultrasound Matrix Imaging.
II. The distortion matrix for aberration correction over multiple isoplanatic patches.

William Lambert,[1,2] Laura A. Cobus,[1,3] Mathias Fink,[1] and Alexandre Aubry[1,*]

[1] *Institut Langevin, ESPCI Paris, CNRS, PSL University, 1 rue Jussieu, 75005 Paris, France*
[2] *SuperSonic Imagine, Les Jardins de la Duranne, 510 Rue René Descartes, 13857 Aix-en-Provence, France*
[3] *Dodd-Walls Centre for Photonic and Quantum Technologies and Department of Physics, University of Auckland, Private Bag 92019, Auckland 1010, New Zealand*

This is the second article in a series of two which report on a matrix approach for ultrasound imaging in heterogeneous media. This article describes the quantification and correction of aberration, i.e. the distortion of an image caused by spatial variations in the medium speed-of-sound. Adaptive focusing can compensate for aberration, but is only effective over a restricted area called the isoplanatic patch. Here, we use an experimentally-recorded matrix of reflected acoustic signals to synthesize a set of virtual transducers. We then examine wave propagation between these virtual transducers and an arbitrary correction plane. Such wave-fronts consist of two components: (*i*) An ideal geometric wave-front linked to diffraction and the input focusing point, and; (*ii*) Phase distortions induced by the speed-of-sound variations. These distortions are stored in a so-called distortion matrix, the singular value decomposition of which gives access to an optimized focusing law at any point. We show that, by decoupling the aberrations undergone by the outgoing and incoming waves and applying an iterative strategy, compensation for even high-order and spatially-distributed aberrations can be achieved. As a proof-of-concept, ultrasound matrix imaging (UMI) is applied to the *in-vivo* imaging of a human calf. A map of isoplanatic patches is retrieved and is shown to be strongly correlated with the arrangement of tissues constituting the medium. The corresponding focusing laws yield an ultrasound image with an optimal contrast and a transverse resolution close to the ideal value predicted by diffraction theory. UMI thus provides a flexible and powerful route towards computational ultrasound.

In most ultrasound imaging, the human body is insonified by a series of incident waves. The medium reflectivity is then estimated by detecting acoustic backscatter from short-scale variations of the acoustic impedance. An image (spatial map) of reflectivity is commonly constructed using delay-and-sum beamforming (DAS). In this process, echoes coming from a particular point, or image pixel, are selected by computing the time-of-flight associated with the forward and return travel paths of the ultrasonic wave between the probe and that point. A sum over all of these echoes is placed at the corresponding spot (pixel) of the image, and the procedure repeated for each pixel. In clinical ultrasound, real-time imaging requires a low computational burden; thus, the time-of-flight between any incident wave and focal point is calculated with the assumption that the medium is homogeneous with a constant speed-of-sound. However, in human tissue, long-scale fluctuations of the acoustic impedance can invalidate this assumption [1]. The resulting incorrectly calculated times-of-flight (also called focusing laws) can lead to aberration of the associated image, meaning that resolution and contrast are strongly degraded. While adaptive focusing methods have been developed to deal with this issue, they rely on the hypothesis that aberrations do not change over the entire field-of-view. However, this assumption is simply incorrect in soft tissues [2] such as fat, skin and muscle, in which the order of magnitude of acoustic impedance fluctuations is around 5% [3]. This causes higher-order aberrations which are only invariant over small regions, often referred to as *isoplanatic patches.* To tackle this issue, recent studies [4, 5] extract an aberration law for each image voxel by probing the correlation of the time delayed echoes coming from adjacent focal spots. The aberration laws are estimated either in the time domain [4–7] or in the Fourier domain [8], for different insonification sequences (focused beams [6, 7], single-transducer insonification [5] or plane wave illumination [4]). In all of these techniques, a focusing law is estimated in either the receive [6, 8] or transmit [5] mode, but this law is then used to compensate for aberrations in both reflection and transmission. However, spatial reciprocity between input and output is only valid if the emission and detection of waves are performed in the same basis; in other words, the distortion undergone by a wavefront travelling to and from a particular point is only the same if the wave has interacted with the same heterogeneities in both directions. If this condition is not fulfilled, applying the same aberration phase law in transmit and receive modes may improve the image quality to some degree, but will not be optimal.

To obtain optimized focusing laws both in transmit and receive modes, these two steps must be considered separately. Recent studies [9–11] have shown how to decouple the location of the transmit and receive focal spots to build a focused reflection (FR) matrix $\mathbf{R}$. Containing the medium responses between virtual sources and vir-

* alexandre.aubry@espci.fr

tual sensors located within the medium, this matrix is the foundation of ultrasound matrix imaging (UMI). Firstly, a focusing criterion can be built from the FR matrix, which allows the mapping of the focusing quality over all pixels of the ultrasound image [12] in both speckle and specular regimes [9]. Secondly, the distortion matrix **D** can be built from the FR matrix for a local correction of high-order aberrations; this concept was first presented in optical imaging [13], then in ultrasound [14], and most recently in seismology [15]. Whereas **R** holds the wavefronts which are reflected from the medium, **D** contains the deviations from an ideal reflected wavefront which would be obtained in the absence of heterogeneities. It has been shown that, for specular reflectors [13], in sparse media [15] and in the speckle regime [14], a time reversal analysis of **D** yields a one-to-one association between each isoplanatic patch in the focal plane and the corresponding wavefront distortion in the far-field. While this promising method shows some similarities with other works [4, 5, 8, 16], the FR matrix here plays a pivotal role. A set of distortion matrices can be built from **R** by projecting the input or output wave-fields towards different bases for an optimal aberration correction (far-field, transducer plane, some intermediate surface, *etc.*). A local aberration correction is then obtained by adjusting the field-of-view covered by the virtual transducers with each isoplanatic patch. In practice, an iterative procedure is applied by reducing gradually the size of the isoplanatic patches, thereby compensating for more and more complex aberrations throughout the iteration process. Note that, experimentally, UMI only requires the recording of a reflection matrix – all subsequent steps are performed in post-processing.

Here we apply UMI to the complex case of *in-vivo* imaging of a human calf. In an previous article, we presented the basic idea and an experimental proof-of-concept of the distortion matrix approach [14]. The current article describes how to implement UMI in *in-vivo* conditions. Each step of the procedure is given in detail, and the physical mechanism hidden behind the calculations are discussed. While our previous paper was limited to an aberration correction from the Fourier plane [14], the distortion matrix approach is here described in the transducer basis. The aberration correction process is then successively performed in the plane wave and transducer bases, at input and output and by gradually reducing the size of the addressed isoplanatic patches. A set of optimized focusing laws is finally obtained for each point of the medium, enabling (i) a mapping of the isoplanatic patches in the field-of-view, revealing the arrangement of the different tissues in the medium, and (ii) the calculation of an ultrasound image with optimal contrast and close-to-ideal resolution over the whole field-of-view. The drastic improvement compared to the conventional ultrasound image is quantified by means of the focusing $F-$factor introduced in the first paper of the series [12]. The aberration correction strategy described in this work is by no means exhaustive, and can be adapted according to the experimental conditions and the nature of aberrations. In the following, we detail various capabilities of this approach, demonstrating the flexibility of UMI.

I. THE FOCUSED REFLECTION MATRIX

A. Experimental procedure

The experimental aspect of our matrix approach consists in recording the reflection matrix **R** using a standard plane wave sequence[17]. The probe was placed in direct contact with the calf of a healthy volunteer, oriented orthogonally with respect to the muscle fibers (this study is in conformation with the declaration of Helsinki. The acquisition was performed using a medical ultrafast ultrasound scanner (Aixplorer Mach-30, Supersonic Imagine, Aix-en-Provence, France) driving a $2-10$ MHz linear transducer array containing 192 transducers with a pitch $p = 0.2$ (SL10-2, Supersonic Imagine). The ultrasound sequence consisted in transmitting 101 steering angles spanning from -25^o to 25^o, calculated assuming a constant speed of sound $c_0 = 1580$ m/s [3] . The emitted signal was a sinusoidal burst of three half periods of the central frequency $f_c = 7.5$ MHz, with pulse repetition frequency 1000 Hz. For each excitation, the back-scattered signal was recorded by all probe elements over time $\Delta t = 80$ μs with a sampling frequency $f_s = 40$ MHz. Mathematically, we write this set of acoustic responses as $\mathbf{R}_{u\theta}(t) \equiv [R(u_{\rm out}, \theta_{\rm in}, t)]$, where $u_{\rm out}$ defines the coordinate of the receiving transducer, $\theta_{\rm in}$ the angle of incidence and t the time-of-flight. Subscripts 'in' and 'out' denote propagation in the forward and backward directions, respectively. Note that the coefficients of $\mathbf{R}_{u\theta}$ should be complex, as they contain the amplitude and phase of the medium response. If the responses $\mathbf{R}_{\mathbf{u}\theta}(t)$ are not complex modulated RF signals, then the corresponding analytic signals should be considered.

B. Computing the focused reflection matrix

In conventional ultrasound imaging, the reflectivity of a medium at a given point is estimated by (i) focusing a wave on this point, thereby creating a virtual source, and (ii) coherently summing the echoes coming from that same point, thus synthesizing a virtual transducer at that location. In UMI, this focusing operation is performed in post-processing, and the input/output focusing points, $\mathbf{r}_{\rm in}/\mathbf{r}_{\rm out}$, are decoupled [Fig. 1(a)]. This is the principle of the broadband focused reflection matrix $\overline{R}_{\mathbf{rr}} = \overline{R}(\mathbf{r}_{\rm in}, \mathbf{r}_{\rm out})$ containing the responses between virtual sources and sensors located throughout the medium. In the first article of this series [12], the FR matrix was built using a beamforming process in the temporal Fourier domain. Here, we show that this matrix can be directly computed in the time domain via conventional

DAS beamforming:

$$\overline{R}(\mathbf{r}_{\text{out}},\mathbf{r}_{\text{in}}) = \sum_{\theta_{\text{in}},u_{\text{out}}} A(u_{\text{out}},\theta_{\text{in}},\mathbf{r}_{\text{in}},\mathbf{r}_{\text{out}}) \\ R(u_{\text{out}},\theta_{\text{in}},t-\tau_{\text{in}}(\theta_{\text{in}},\mathbf{r}_{\text{in}})-\tau_{\text{out}}(u_{\text{out}},\mathbf{r}_{\text{out}})), \quad (1)$$

where τ_{in} and τ_{out} are the transmit and receive focusing laws such that

$$\tau_{\text{in}}(\theta_{\text{in}},\mathbf{r}_{\text{in}}) = [x_{\text{in}}\sin(\theta_{\text{in}}) + z_{\text{in}}\cos(\theta_{\text{in}})]/c_0, \text{ and} \quad (2a)$$

$$\tau_{\text{out}}(u_{\text{out}},\mathbf{r}_{\text{out}}) = \sqrt{|x_{\text{out}}-u_{\text{out}}|^2 + z_{\text{out}}^2}/c_0. \quad (2b)$$

A is an apodization factor that limits the extent of the receive synthetic aperture, and $(x_{\text{in}}, z_{\text{in}})$ and $(x_{\text{out}}, z_{\text{out}})$ are the coordinates of the input and output focusing points $\mathbf{r}_{\text{in}}$ and $\mathbf{r}_{\text{out}}$, respectively. In this paper, we will restrict our study to the $x-$projection of $\overline{\mathbf{R}}_{\mathbf{rr}}$, written $\overline{\mathbf{R}}_{xx}(z)$, in which only the responses between virtual transducers located at the same depth are considered ($z = z_{\text{in}} = z_{\text{out}}$).

C. Manifestation of aberrations and multiple scattering

Each row of $\overline{\mathbf{R}}_{xx}(z)$ corresponds to the situation in which waves have been focused at $\mathbf{r}_{\text{in}} = (x_{\text{in}}, z)$ in transmission, and virtual detectors at $\mathbf{r}_{\text{out}} = (x_{\text{out}}, z)$ record the resulting spatial wave spreading across the focal plane [Fig. 1(a)]. Fig. 1(b) shows $\overline{\mathbf{R}}_{xx}(z)$ at $z = 28$ mm. Note that the coefficients $\overline{R}(x_{\text{out}}, x_{\text{in}})$ associated with a transverse distance $|x_{\text{out}} - x_{\text{in}}|$ larger than a superior bound $\Delta x_{\max} \sim \lambda_{\max}/(2\delta\theta)$ are not displayed because of spatial aliasing [12]. The diagonal coefficients of this matrix correspond to a confocal configuration in which the virtual transducers are exactly at the same position. Thus, the intensity distribution along the diagonal of $\overline{\mathbf{R}}_{xx}(z)$ yields a line of the multi-focus image, $\mathcal{I}(\mathbf{r}) \equiv \left|\overline{R}(\mathbf{r},\mathbf{r})\right|^2$, that would be obtained by plane wave synthetic beamforming [17] [see Fig. 2(a)]. In the single scattering approximation, the impact of aberration on the FR matrix can be expressed theoretically as follows [12]:

$$\overline{R}(x_{\text{out}},x_{\text{in}}) = \int dx H_{\text{out}}(x,x_{\text{out}},z)\gamma(x,z)H_{\text{in}}(x,x_{\text{in}},z) \quad (3)$$

where $\gamma(x,z)$ is the medium reflectivity. $H_{\text{in}}(x,x_{\text{in}},z)$ and $H_{\text{out}}(x,x_{\text{out}},z)$ are the transmit and receive PSFs, *i.e.* the spatial amplitude distribution of the input and output focal spots at depth z.

In the accompanying paper [12], the intensity of the antidiagonals of $\overline{\mathbf{R}}_{xx}(z)$, referred to as the common midpoint (CMP) intensity profile, is shown to give access to the local input-output incoherent PSF, $|H_{\text{in}}|^2 \overset{\Delta x}{\circledast} |H_{\text{out}}|^2$ independently from the medium reflectivity (The symbol $\circledast$ here stands for a convolution product). Fig. 1(g) shows the CMP intensity profile at $z = 28$ mm. A confocal peak can be observed, originating from single scattering, which sits on wider incoherent background from multiple scattering. By comparing the full width at half maximum (FWHM) $\overline{w}(\mathbf{r})$ of the CMP intensity profile with the ideal diffraction-limited value $\overline{\delta x}_0$, a focusing factor $F(\mathbf{r})$ can be defined [12]. Fig. 2(e) shows the $F-$map associated with the image of the human calf. Blue areas $[F(\mathbf{r}) \sim 1)]$ indicate high reliability; the image accurately describes the medium reflectivity. Yellow areas $[F(\mathbf{r}) < 0.5]$ indicate aberrated areas of the image . Gray areas correspond to the situation where the close diagonal coefficients of the FR matrix show no intensity enhancement due to single scattering, preventing the measurement of input-output resolution. This occurs when the intensity level of the backscattered signal generated by the region of interest is lower than the multiple scattering and/or electronic noise contributions. This low intensity level could be due to a weak reflectivity of the medium in the probed region and/or strong fluctuations of the speed-of-sound upstream of the focal plane which decrease the relative single scattering level close to the diagonal. Thus, prior to performing aberration correction, it is important to remove as much multiple scattering background as possible from the FR matrix.

D. Filtering multiple scattering and noise

The multiple scattering contribution to $\overline{\mathbf{R}}_{xx}$ can be suppressed using an adaptive confocal filter [10, 11]. This process consists in weighting the coefficients $\overline{R}(x_{\text{in}}, x_{\text{out}}, z)$ of the FR matrix as a function of the distance $|x_{\text{out}} - x_{\text{in}}|$ between the virtual transducers, such that:

$$R'(x_{\text{out}},x_{\text{in}}) = \overline{R}(x_{\text{out}},x_{\text{in}}) \exp\left[-\frac{|\,x_{\text{out}}-x_{\text{in}}\,|^2}{2l_c^2(\mathbf{r})}\right]. \quad (4)$$

This filter has a Gaussian shape, with a width $l_c(\mathbf{r})$ that needs to be carefully set. If $l_c(\mathbf{r})$ is too large, the multiply-scattered echoes will prevent a correct estimation of the aberration phase law. If $l_c(\mathbf{r})$ is too small, the filter then acts as an apodization function that will smooth out the resulting aberration phase law. To be efficient, $l_c(\mathbf{r})$ should thus match the input-output resolution $\overline{w}(\mathbf{r})$. For areas in which this estimation fails [gray areas in Fig. 2(e)], $l_c(\mathbf{r})$ is set arbitrarily to $n\overline{\delta x}_0(\mathbf{r})$, with n an integer whose value is reported in Table. I.

Figs. 1(b,c) show the original and filtered FR matrices, $\overline{\mathbf{R}}_{xx}$ and $\mathbf{R}'_{xx}$, respectively, computed at $z = 28$ mm. It can be seen that the adaptive confocal filter has removed part of the multiple scattering contribution. However, $\mathbf{R}'_{xx}$ still contains a residual multiple scattering component which exists at matrix coefficients very close to the diagonal. Note that this filter has no impact on the raw ultrasound image since the confocal signals are unaffected. However, it constitutes a necessary step for the determination of the aberration law as it greatly improves

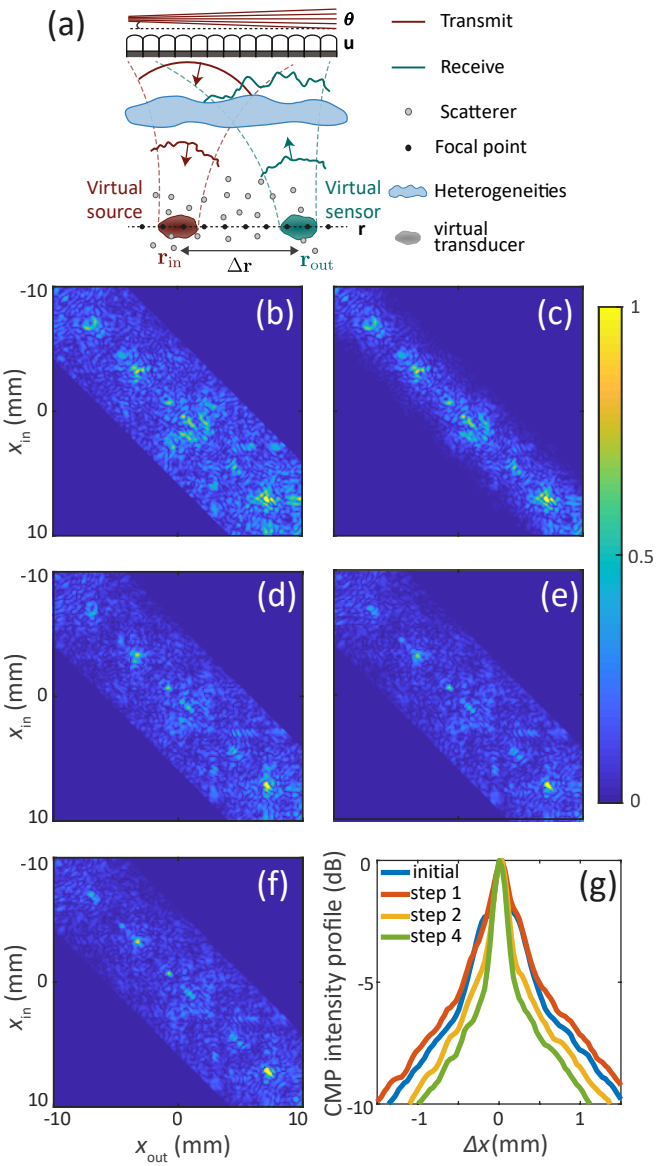

FIG. 1. Focused reflection matrix. (a) UMI consists in splitting the locations of the transmit ($\mathbf{r}_{\text{in}}$) and receive ($\mathbf{r}_{\text{out}}$) focusing points. (b)-(f) Evolution of $\mathbf{R}_{xx}(z)$ at depth z = 28 mm during the aberration correction process. $\overline{\mathbf{R}}_{xx}$ is shown (b) prior to correction, (c) after the application of the adaptive confocal filter (4), (d) after aberration correction in the $(u_{\text{out}}, \theta_{\text{in}})$ bases, (e) after aberration correction in the $(u_{\text{in}}, \theta_{\text{out}})$ bases, and (f) after the ultimate correction based on the normalized correlation matrix $\hat{\mathbf{C}}$. (g) Evolution of the corresponding CMP intensity profiles $I(\mathbf{r}, \Delta x)$ spatially averaged over the area $\mathcal{A}_1$ [Fig. 2(a)].

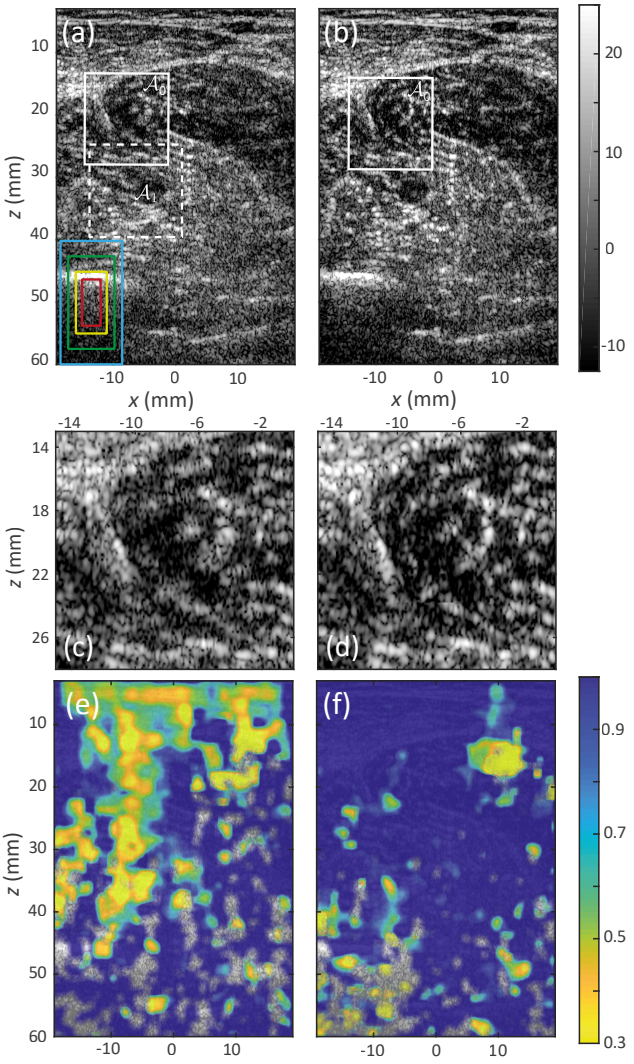

FIG. 2. Results of the aberration correction process applied to *in-vivo* imaging of the human calf. (a) Conventional multi-focus image. The dashed white square $\mathcal{A}_1$ defines the area used to estimate the average CMP intensity profiles shown in Fig. 1(g). The four solid, colored rectangles correspond to the spatial windows $W_{\Delta\mathbf{r}}$ used in the four steps of the correction process (from the largest to smallest, see Table.I).(b) Corrected multi-focus UMI image. (c,d) Zooms of the initial and corrected images [white rectangles $\mathcal{A}_0$ in (a) and (b)]. (e,f) Focusing criterion superimposed onto the (e) conventional and (f) corrected images.

the signal-to-noise ratio (SNR).

II. MATRIX CORRECTION OF ABERRATIONS

The FR matrix $\mathbf{R}'_{xx}(z)$ is now used to implement the distortion matrix concept [14]. In this section, we will show how to estimate and correct for aberrations successively and independently in the transmit and receive modes, both from the far-field and the surface of the transducer array. We describe all of the technical steps of the aberration correction process: (i) the projection of the FR matrix at output or input into a correction ba-

TABLE I. Parameters used for the UMI process.

Correction steps	1	2	3	4
$n = l_c/\overline{\delta x}_0$	10	10	8	6
Δx (mm)	10	7.5	5	3
Δz (mm)	20	15	10	7.5
Transmit basis	k_{in}	u_{in}	k_{in}	u_{in}
Receive basis	u_{out}	k_{out}	u_{out}	k_{out}
SVD type	$\mathbf{D}$	$\mathbf{D}$	$\hat{\mathbf{C}}$	$\hat{\mathbf{C}}$

sis (here either the Fourier or transducer basis) in order to investigate the reflected or incident wave-front associated with each virtual source or transducer, respectively, (*ii*) the realignment of the transmitted or reflected wavefronts to form the distortion matrix $\mathbf{D}$, (*iii*) the truncation of $\mathbf{D}$ into overlapping isoplanatic patches, (*iv*) the singular value decomposition of $\mathbf{D}$ or of its normalized correlation matrix to extract an aberration phase law for each isoplanatic patch, and (*v*) the application of the focusing law and back-projection of the reflection matrix into the focused basis. All of these steps are repeated by exchanging input and output bases, as well as the correction basis (See Supplementary Fig. S1). The process can then be iterated while gradually reducing the size of isoplanatic patches in order to address higher order aberrations.

A. Projection of the reflection matrix into a dual basis

In adaptive focusing, the aberrating layer is often modeled as a random phase screen. For an optimal correction, the ultrasonic data should be back-propagated to the plane containing this aberrating layer; indeed, in this plane, the aberration is spatially-invariant. By applying the phase conjugate of the aberration phase law, aberration can be fully compensated for at any point of the medium. However, in real life, speed-of-sound inhomogeneities are distributed over the entire medium and aberration can take place everywhere. To treat this case, the strategy here is to back-propagate ultrasound data into several planes from which the aberration phase law should be estimated and then compensated. The optimal correction plane is the one that maximizes the size of isoplanatic patches. For multi-layered media, the Fourier plane is the most adequate since plane waves are the propagation invariants in this geometry. For aberrations induced by superficial veins or skin nodules, the probe plane is a good choice. In this paper, the aberration correction will be performed in these two planes as they coincide also to the emission and reception bases used to record the reflection matrix. However, note that, in practice, other correction planes can be chosen according to the imaging problem.

1. *Projection into the far-field*

To project the reflected wave-field into the far-field, a spatial Fourier transform should be applied to the output of $\mathbf{R}'_{xx}(z)$:

$$\mathbf{R}'_{kx}(z) = \mathbf{T_0} \times \mathbf{R}'_{xx}(z). \tag{5}$$

where $\mathbf{T_0}$ is the Fourier transform operator

$$T_0(k_x, x) = \exp\left(ik_x x\right), \tag{6}$$

k_x the transverse wave number, and $\mathbf{R}'_{kx}(z) \equiv [R(k_{\text{out}}, x_{\text{in}}, z)]$ contains the set of far-field aberrated wavefronts generated by each virtual source $\mathbf{r}_{\text{in}}$. Fig. 3(a) shows the phase of $\mathbf{R}'_{kx}(z)$ at $z = 55$ mm. Using the central frequency f_c as a reference frequency, the transverse wave number k_{out} can be associated with a plane wave of angle θ_{out}, such that $k_{\text{out}} = k_c \sin(\theta_{\text{out}})$, with $k_c = 2\pi f_c/c_0$. Expressing the far-field projection as a plane wave decomposition is useful to define the boundaries of this basis [white dashed lines in Fig. 3(a)]; the maximum transverse wave number is $k_{\max} \sim k_c \sin[\beta(\mathbf{r})]$, where $\beta(\mathbf{r})$ the maximum angle of wave illumination (in transmit mode) or collection (in receive mode) by the array from the associated focal point [see Fig. 3(l)].

The matrix $\mathbf{R}'_{kx}(z)$ will be used to tackle aberrations in the receive plane wave basis. To do the same in the transmit basis, a reciprocal projection to that of (5) can be performed at the input of $\mathbf{R}'_{xx}(z)$:

$$\mathbf{R}'_{xk}(z) = \mathbf{R}'_{xx}(z) \times {\mathbf{T_0}}^{\top}. \tag{7}$$

where the symbol $\top$ stands for matrix transpose. The coefficients $R'(x_{\text{out}}, k_{\text{in}}, z)$ correspond to the wave-field probed by the virtual transducer at $\mathbf{r}_{\text{out}}$ if a plane wave of transverse wave number k_{in} illuminates the medium. This matrix will be used to investigate aberrations in the transmit plane wave basis.

2. *Projection into the transducer basis*

The strategy to treat aberrations in the transducer plane is similar to that described above. Free-space transmission matrix $\mathbf{Q}_0$ is defined between the focused and transducer bases at central frequency f_c:

$$\mathbf{Q}_0 = \mathbf{T}_0^{-1} \times (\mathbf{P} \circ \mathbf{T}_0), \tag{8}$$

where the symbol $\circ$ stands for a Hadamard product and $\mathbf{P} = [P(k_x, z)]$ is the plane wave propagator at the central frequency: $P(k_x, z) = e^{i\sqrt{k_c^2 - k_x^2}z}$. The operator $\mathbf{Q}_0$ can

be given a physical interpretation by reading the terms of (8) from right to left: (i) a spatial Fourier transform using the operator $\mathbf{T}_0$ to project the wave-field in the plane wave basis; (ii) the plane wave propagation modeled by the propagator $\mathbf{P}$ between the focal and transducer planes over a distance z; (iii) an inverse Fourier transformation $\mathbf{T}_0^{-1}$ that projects the wave-field into the transducer basis. To clarify the physical meaning of this operator, its coefficients can be expressed under the Fresnel approximation as follows:

$$Q_0(\mathbf{r},u) \approx e^{ik_c z} e^{ik_c x^2/(2z)} e^{ik_u(u-x)}, \tag{9}$$

where $k_u = k_c u/z$ can be seen as a transverse wave number. Using this operator $\mathbf{Q}$, the matrix $\mathbf{R}'_{xx}$ can be projected into the transducer basis either at input,

$$\mathbf{R}'_{xu}(z) = \mathbf{R}'_{xx}(z) \times \mathbf{Q_0}^{\top} \tag{10}$$

or output,

$$\mathbf{R}'_{ux}(z) = \mathbf{Q_0} \times \mathbf{R}'_{xx}(z). \tag{11}$$

Each column of $\mathbf{R}'_{xu}(z) = [R(x_{\text{out}}, u_{\text{in}}, z)]$ holds the wave-field received by the virtual transducer at $\mathbf{r}_{\text{out}}$ for an incident wave-field emitted from a transducer at u_{in}. Reciprocally, each row of $\mathbf{R}'_{ux}(z) = [R(u_{\text{out}}, x_{\text{in}}, z)]$ contains the wave-front recorded by the transducers for a virtual source in the focal plane at $\mathbf{r}_{\text{in}}$. Fig. 3(b) shows the phase of $\mathbf{R}'_{ux}(z)$ obtained at $z = 55$ mm. At this relatively large depth, the spatial extension Δu of the reflected wave-field in the transducer basis coincides with the physical aperture A of the array used to collect the echoes coming from a depth z. In contrast, Fig. 3(l) demonstrates that for shallower depths $z < A\tan[\beta(\mathbf{r})]/2$, Δu is limited by the numerical aperture of the probe such that $\Delta u \sim 2z\tan[\beta_{\max}]$.

3. *Discussion*

We might expect to observe correlations between the columns of matrices $\mathbf{R}'_{kx}(z)$ and $\mathbf{R}'_{ux}(z)$ displayed in Figs. 3(a)-(b). Because neighboring virtual sources $\mathbf{r}_{\text{in}}$ belong *a priori* to the same isoplanatic patch, the associated wave-fronts observed in the transducer plane or in the far-field should thus be, in principle, strongly correlated since they travel through the same area of the aberrating layer. However, such correlations are not obvious by eye in Figs. 3(a)-(b). In the following, we show how to reveal these hidden correlations by introducing the distortion matrix. We will consider mostly the transducer basis, as the far-field case has already been explored in a previous work [14].

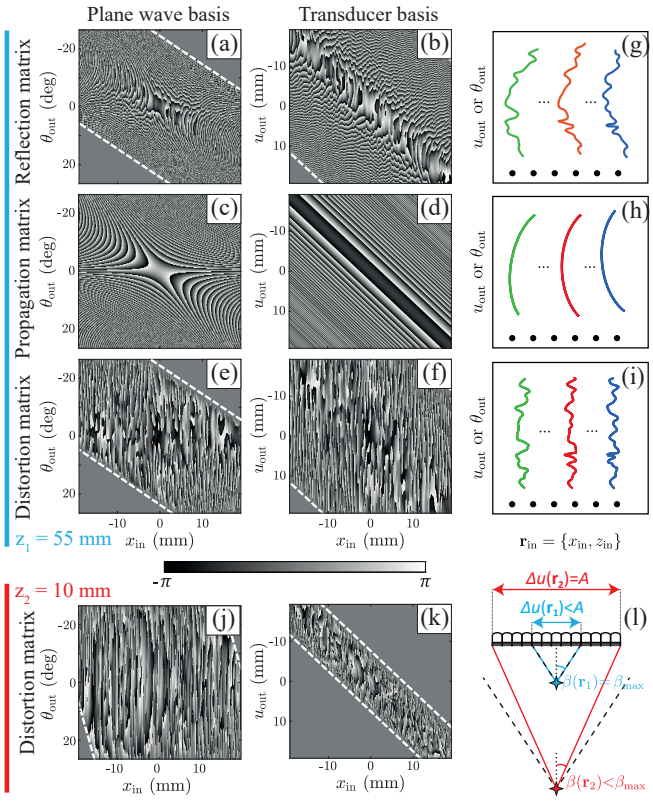

FIG. 3. Revealing the spatial correlations between reflected wave-fields. The first and second columns correspond to the analysis of the reflected wave-fronts in the plane wave and transducer bases, respectively. By subtracting the phase of the dual reflection matrices, $\mathbf{R}'_{kx}$ (a) and $\mathbf{R}'_{ux}$ (b), from their geometrical counterpart, the free-space propagation matrices $\mathbf{P_0}$ (c) and $\mathbf{T_0}$ (d), the distortion matrices, $\mathbf{D}_{kx}$ (e) and $\mathbf{D}_{kx}$ (f), reveal the long-range spatial correlations which exist in the reflected wavefield associated with each isoplanatic patch. (g,h,i) Sketch of the wave-fronts contained the reflection (a,b), free-space (c,d) and distortion (e,f) matrices, respectively. The matrices shown in panels (a)-(f) correspond to a depth of $z = 55$ mm. (j,k) The phase of the distortion matrices are also displayed for $z = 10$ mm. (l) The white dashed lines in panels (a)-(f) and (j)-(k) account for the finite angular extent $\beta(\mathbf{r})$ and spatial support $\Delta u(\mathbf{r})$ of the reflected waves in the plane wave and transducer bases, respectively.

B. The distortion matrix

To reveal the isoplanaticity of the reflected wave-field, each aberrated wave-front contained in the reflection matrix $\mathbf{R}'_{ux}(z)$ [Fig. 3(g)] should be decomposed into two components: (*i*) a geometric component described by $\mathbf{Q}_0(z)$, which contains the ideal wave-front induced by the virtual source $\mathbf{r}_{\text{in}}$ that would be obtained in the homogeneous medium used to model the wave propagation [Fig. 3(h)]; (*ii*) a distorted component due to the mismatch between the propagation model and reality [Fig. 3(i)]. A key idea is to isolate the latter contribution by subtracting, from the experimentally measured wave-

front, its ideal counterpart. Mathematically, this operation can be done by means of an Hadamard product between $\mathbf{R}'_{ux}(z)$ and $\mathbf{Q}_0^*(z)$:

$$\mathbf{D}_{ux}(z) = \mathbf{R}'_{ux}(z) \circ \mathbf{Q}_0^*(z). \tag{12}$$

where the symbol $*$ stands for phase conjugate. We call $\mathbf{D}_{u\mathbf{r}} = \mathbf{D}_{ux}(z) = [D(u_{\rm out}, \{x_{\rm in}, z\})]$ the *distortion matrix*. It connects any input focal point $\mathbf{r}_{\rm in}$ to the distorted component of the reflected wavefield in the transducer basis. Using (9), the coefficients of the distortion matrix can be written in the Fraunhoffer approximation as [18]:

$$D(u_{\rm out}, \{x_{\rm in}, z\}) = \sum_{\delta x} R'(x_{\rm in} + \delta x, x_{\rm in}, z) e^{i\frac{k_c}{2z} u_{\rm out} \delta x}, \tag{13}$$

with $\delta x = x_{\rm out} - x_{\rm in}$. Mathematically, each column of $\mathbf{D}_{u\mathbf{r}}$ is the Fourier transform of the focused wave-field re-centered around each focusing point $\mathbf{r}_{\rm in}$. $\mathbf{D}_{u\mathbf{r}}$ can thus be seen as a dual reflection matrix for different realizations of virtual sources, all shifted at the origin of the focal plane ($x_{in} = 0$) [14] (See Supplementary Fig. S3) . The co-location of the virtual sources at the same point is the reason why the columns of $\mathbf{D}_{ux}(z)$ [Fig. 3(f)] are much more highly correlated than those of $\mathbf{R}'_{ux}(z)$ [Fig. 3(b)].

Note that equivalent distortion matrices, $\mathbf{D}_{\mathbf{r}u}$, $\mathbf{D}_{k\mathbf{r}}$ and $\mathbf{D}_{\mathbf{r}k}$ can be built from the other reflection matrices previously defined: $\mathbf{R}'_{xu}(z)$, $\mathbf{R}'_{kx}(z)$ and $\mathbf{R}'_{xk}(z)$. For $\mathbf{D}_{\mathbf{r}u}$, the same reasoning as above can be used by exchanging input and output. The far-field distortion matrices, $\mathbf{D}_{k\mathbf{r}}$ and $\mathbf{D}_{\mathbf{r}k}$ have already been investigated in a previous work [14]. The comparison between the phase of $\mathbf{R}'_{kx}(z)$ [Fig. 3(a)] and $\mathbf{D}_{kx}(z)$ [Fig. 3(e)] highlights the high degree of correlation of the distorted wave-fields in the far-field, resulting from the virtual shift of all the input focal spots to the origin.

C. Local distortion matrices

We have shown that virtual sources which belong to the same isoplanatic patch should give rise to strongly correlated distorted wave-fronts, even if the reflectivity of the medium is random [see Figs. 3(e,f)]. To correct for multiple isoplanatic patches in the field-of-view, recent works [13, 14] show that the distortion matrix can be analyzed over the whole field-of-view. Its effective rank is then equal to the number of isoplanatic patches contained in this field-of-view, while its singular vectors yield the corresponding aberration phase laws. The proof-of-concept of this fundamental result was first demonstrated in optics for specular reflectors [13], then in ultrasound speckle for multi-layered media [14] and lately in seismic imaging for sparse media [15].

Here, we investigate the case of ultrasound *in vivo* imaging, in which fluctuations of the speed-of-sound occur both in the lateral and axial directions. This means that the spatial distribution of aberration effects can become more complex. In Fig. 2(e), strong fluctuations of the F-map illustrate the complexity of the speed-of-sound distribution in the human calf. Such complexity implies that any point in the medium will be associated with its own distinct aberration phase law. To construct an image in these conditions, the transmission matrix connecting the correction and focused bases should therefore be constructed to include all of these phase laws – an extremely difficult task. Here, this problem will be tackled using an analysis of a *local* distortion matrix. The idea is to take advantage of the local isoplanicity of the aberration phase law around each focusing point.

To begin, we divide the field-of-illumination into overlapping regions that are defined by their central midpoint $\mathbf{r}_{\rm p}$ and their spatial extension $\Delta\mathbf{r} = \{\Delta x, \Delta z\}$. All of the distorted components associated with focusing points $\mathbf{r}_{\rm in}$ located within each region are extracted and stored in a local distortion matrix $\mathbf{D}'_{u\mathbf{r}}(\mathbf{r}_{\rm p})$:

$$D'(u_{\rm out}, \mathbf{r}_{\rm in}, \mathbf{r}_{\rm p}) = D(u_{\rm out}, \mathbf{r}_{\rm in})\ W_{\Delta\mathbf{r}}(\mathbf{r}_{\rm in} - \mathbf{r}_{\rm p}), \tag{14}$$

where $W_{\Delta\mathbf{r}}(\mathbf{r}) = 1$ for $|x| < \Delta x$ and $|z| < \Delta z$, and zero otherwise. Ideally, each sub-distortion matrix should contain a set of focusing points $\mathbf{r}_{\rm in}$ belonging to the same isoplanatic patch. In reality, the isoplanicity condition is never completely fulfilled. A delicate compromise thus has to be made on the size $\Delta\mathbf{r}$ of the window function: it must be small enough to approach the isoplanatic condition, but large enough to encompass a sufficient number of independent realizations of disorder [14]. This last point is discussed in Sec. II E.

D. Isoplanicity

For sake of analytical tractability, the isoplanatic condition is assumed to be fulfilled over each region of size $\Delta\mathbf{r}$. This hypothesis implies that the PSFs $H_{\rm in}$ and $H_{\rm out}$ are invariant by translation in each region: $H_{\rm in/out}(x', x, z) = H_{\rm in/out}(x' - x, z, \mathbf{r}_{\rm p})$. Injecting (3) into (13) leads to the following expression for the $\mathbf{D}$-matrix coefficients:

$$D'(u_{\rm out}, \mathbf{r}_{\rm in}, \mathbf{r}_{\rm p}) = \tilde{H}_{\rm out}(u_{\rm out}, \mathbf{r}_{\rm p}) \int dx \gamma(x + x_{\rm in}, z) H_{\rm in}(x, \mathbf{r}_{\rm p}) e^{i\frac{k_c}{2z} u_{\rm out} x}. \tag{15}$$

The physical meaning of this last equation is the following: Around each point $\mathbf{r}_{\rm p}$, the aberrations can be modelled by a transmittance $\tilde{H}_{\rm out}(u_{\rm out}, \mathbf{r}_{\rm p})$. This transmittance is the Fourier transform of the output PSF $H_{\rm out}(x, \mathbf{r}_{\rm p})$:

$$\tilde{H}_{\rm out}(u_{\rm out}, \mathbf{r}_{\rm p}) = \sum_x H_{\rm out}(x, \mathbf{r}_{\rm p}) e^{-i\frac{k_c}{2z} u_{\rm out} x}. \tag{16}$$

The aberration matrix $\tilde{\mathbf{H}}_{\text{out}}$ directly provides the *true* transmission matrix $\mathbf{Q}$ between the transducers and any point $\mathbf{r}_\text{p}$ of the medium:

$$\mathbf{Q} = \tilde{\mathbf{H}}_{\text{out}} \circ \mathbf{Q}_0. \tag{17}$$

This transmission matrix $\mathbf{Q}$, or equivalently the aberration matrix $\tilde{\mathbf{H}}_{\text{out}}$, are the holy grail for ultrasound imaging since their phase conjugate directly provides the focusing laws that need to be applied on each transducer to optimally focus on each point $\mathbf{r}_\text{p}$ of the medium.

E. Singular value decomposition

To extract the aberration phase law $\tilde{H}_{\text{out}}(u_{\text{out}}, \mathbf{r}_\text{p})$ from each local distortion matrix, we can notice from (15) that each line of $\mathbf{D}'_{u\mathbf{r}}(\mathbf{r}_\text{p})$ is the product between $\tilde{H}_{\text{out}}(u_{\text{out}}, \mathbf{r}_\text{p})$ and a random term associated with each virtual source. This explains the strong correlation between the columns of $\mathbf{D}'_{u\mathbf{r}}(\mathbf{r}_\text{p})$ in Fig. 3(f). To unscramble the deterministic term $\tilde{H}_{\text{out}}(u_{\text{out}}, \mathbf{r}_\text{p})$ from the random virtual source term in (15), the singular value decomposition (SVD) of $\mathbf{D}'_{u\mathbf{r}}(\mathbf{r}_\text{p})$ can be applied. The SVD consists in writing $\mathbf{D}'_{u\mathbf{r}}(\mathbf{r}_\text{p})$ as

$$\mathbf{D}'_{u\mathbf{r}}(\mathbf{r}_\text{p}) = \mathbf{U}(\mathbf{r}_\text{p}) \times \mathbf{\Sigma}(\mathbf{r}_\text{p}) \times \mathbf{V}^\dagger(\mathbf{r}_\text{p}), \tag{18}$$

where the symbol † stands for transpose conjugate. $\mathbf{\Sigma}$ is a diagonal matrix containing the singular values $\sigma_i(\mathbf{r}_\text{p})$ in descending order: $\sigma_1 > \sigma_2 > .. > \sigma_N$. $\mathbf{U}(\mathbf{r}_\text{p})$ and $\mathbf{V}(\mathbf{r}_\text{p})$ are unitary matrices that contain the orthonormal set of output and input eigenvectors, $\mathbf{U}_i(\mathbf{r}_\text{p}) = [U_i(u_{\text{out}}, \mathbf{r}_\text{p})]$ and $\mathbf{V}_i(\mathbf{r}_\text{p}) = [V_i(\mathbf{r}_{\text{in}}, \mathbf{r}_\text{p})]$. The physical meaning of this SVD can be intuitively understood by considering the asymptotic case of a point-like input focusing beam $[H_{\text{in}}(x) = \delta(x)]$. In this ideal case, (15) becomes $D(u_{\text{out}}, \mathbf{r}_{\text{in}}, \mathbf{r}_\text{p}) = \tilde{H}_{\text{out}}(u_{\text{out}}, \mathbf{r}_\text{p})\gamma(\mathbf{r}_{\text{in}})$. Comparison with (18) shows that $\mathbf{D}'_{u\mathbf{r}}(\mathbf{r}_\text{p})$ is then of rank 1 – the first output singular vector $\mathbf{U}_1(\mathbf{r}_\text{p})$ yields the aberration transmittance $\tilde{\mathbf{H}}_{\text{out}}(\mathbf{r}_\text{p})$ while the first input eigenvector $\mathbf{V}_1(\mathbf{r}_\text{p})$ directly provides the medium reflectivity. In reality, the input PSF H_{in} is of course far from being point-like. The spectrum of $\mathbf{D}'_{u\mathbf{r}}(\mathbf{r}_\text{p})$ displays a continuum of singular values (see Supplementary Section S2) and $\mathbf{V}_1(\mathbf{r}_\text{p})$ only provides a low-resolution image of the medium [15]. Nevertheless, the normalized first output singular vector, $\hat{U}_1(u_{\text{out}}, \mathbf{r}_\text{p}) = U_1(u_{\text{out}}, \mathbf{r}_\text{p})/|U_1(u_{\text{out}}, \mathbf{r}_\text{p})|$, can still constitute a reliable estimator of $\tilde{\mathbf{H}}_{\text{out}}(\mathbf{r}_\text{p})$ in this case. The finite spatial extension $\overline{\delta x}_{\text{in}}$ of the transmitted focal spot degrades the quality of this estimator, but this effect can be mitigated by averaging over a large number of realizations of disorder, i.e. independent input focal points N_{in}. Here, if we assume that aberrations can be modelled by a Gaussian process, a correct estimation of the aberration phase law requires(see Supplementary Section S2):

$$N_{\text{in}} \sim \exp\left[(\overline{\delta x}_{\text{in}}/\overline{\delta x}_0)^2\right]. \tag{19}$$

This condition is quite restrictive and justifies our initial choice for the area $\Delta\mathbf{r}$: $N_{\text{in}} = \Delta x \Delta z/(\overline{\delta x}_0 \delta z_0) \sim 5000$ (see Table I). It also explains why the aberration correction process should then be iterated; at with each iteration, the focal spot size, $\overline{\delta x}_{\text{in}}$ or $\overline{\delta x}_{\text{out}}$, decreases and the spatial window $\Delta\mathbf{r}$ can be reduced accordingly. In the end, the measurement of aberration matrices $\tilde{\mathbf{H}}_{\text{out}}$ and $\tilde{\mathbf{H}}_{\text{in}}$ will thus have excellent spatial resolution.

F. Transmission matrix estimator

1. *Aberration correction in the receive transducer basis*

Now that an estimator $\hat{\mathbf{U}}_1$ of the aberration matrix $\tilde{\mathbf{H}}_{\text{out}}$ has been derived, its phase conjugate can be used as a focusing law to compensate for aberrations. We start by correcting in the transducer basis in receive (output). This means building an estimator $\mathbf{Q_1}$ of the transmission matrix from the Hadamard product of the free space transmission matrix $\mathbf{Q_0}$ and the phase conjugate of $\hat{\mathbf{U}}_1$:

$$\mathbf{Q_1} = \mathbf{Q_0} \circ \hat{\mathbf{U}}_1^*. \tag{20}$$

$\mathbf{Q_1}$ is then used to recalculate the broadband FR matrix $\overline{\mathbf{R}}_{xx}(z)$ (1), leading to a corrected FR matrix $\mathbf{R}^{(c)}_{xx}(z)$:

$$\mathbf{R}^{(c)}_{xx}(z) = \mathbf{Q}_1^\dagger(z) \times \mathbf{Q_0}(z) \times \overline{\mathbf{R}}_{xx}(z). \tag{21}$$

Note that the correction is applied to the raw FR matrix $\overline{\mathbf{R}}_{xx}(z)$, and not to the filtered FR matrix $\mathbf{R}'_{xx}(z)$. This is to make sure that no singly-scattered echo is removed during the aberration correction process.

2. *Aberration correction in the transmit plane wave basis*

Next, aberration correction is performed for the transmit mode (input). It is important to note that it is possible to change the correction basis if need be. Here, correcting in the plane-wave basis in the transmit mode is optimal since the ultrasound emission sequence was performed in this basis. Indeed, it can also help to compensate for unwanted movements of the medium that may have occurred during the acquisition. A set of dual reflection matrices $\mathbf{R}'_{xk}(z)$ (7) is built from the updated FR matrix and an aberration phase law is extracted from the corresponding distortion matrices $\mathbf{D}'_{\mathbf{r}k}(\mathbf{r}_\text{p})$ [14]. The aberration correction process in the plane wave basis is similar to that described here for the transducer basis (20)-(21), replacing the matrix $\mathbf{Q}_0$ by $\mathbf{T}_0$ (6). The result is an updated FR matrix $\mathbf{R}^{(c)}_{xx}(z)$, an example of which is displayed in Fig. 1(e) at $z = 28$ mm. The corresponding CMP intensity profile is displayed in Fig. 1(g) for

TABLE II. Result of the UMI process in the area $\mathcal{A}_1$ [Fig. 2(a)].

Correction step	0	1	2	3/4
F	0.34	0.37	0.73	0.90
w (mm)	0.55	0.51	0.26	0.21
Contrast (dB)	2.4	2.5	4.4	5.4

the area $\mathcal{A}_1$ shown in Fig. 2(a). Compared to the initial CMP intensity profile, the result of this first step of the aberration correction process seems quite modest (see Table. II). This is explained by the relatively large size of the spatial window $\Delta\mathbf{r}$ chosen at the first step of the UMI process (Table. I). While the central part of the FR matrix seems thinner in Fig. 1(d) compared to its initial counterpart in Fig. 1(b), the focusing quality is not drastically improved on the eccentric parts of the field-of-view. This means that the isoplanatic patches are probably smaller than the area $\Delta\mathbf{r}$ of the spatial window whose initial value was fixed to meet the convergence condition of (19).

3. Iteration of the UMI process

The aberration correction process can now be iterated over smaller areas (see Table. I). Note that the correction bases are also exchanged between input and output to minimize any redundancy in the algorithm and optimize the efficiency of this second step. An example of the resulting FR matrix $\mathbf{R}_{xx}^{(c)}(z)$ is displayed for $z = 28$ mm in Fig. 1(e). Compared to the previous step, the majority of the back-scattered energy in $\mathbf{R}_{xx}^{(c)}(z)$ is now concentrated along the diagonal. The CMP intensity profile displayed in Fig. 1(g) illustrates the gain both in terms of resolution and contrast of the input and output PSFs. After this second step, the transverse resolution is actually enhanced by a factor of two in the area $\mathcal{A}_1$ [Fig. 2(a)] and the contrast shows an improvement of 2 dB [see Table. II]. The contrast is here computed as the ratio between the energy at focus, $I(\Delta x = 0)$, and the CMP intensity value at the expected resolution length, $I(\Delta x = \delta x_0)$, with $\delta x_0 = 0.19$ mm in area $\mathcal{A}_1$.

4. Convergence of the UMI process

The iteration of the aberration correction process can then be pursued since the quality of focus is improved at each step. This results in more highly-resolved virtual transducers which, in return, provides a better estimation of the aberration phase law (in particular at large angles in the plane wave basis or near the edge of the array in the transducer basis). To accelerate the convergence of the UMI process and compensate for the residual aberrations more efficiently, it can be useful to consider the normalized correlation matrix $\delta\hat{\mathbf{C}}$ of the residual distortion matrix [15] (see Supplementary Section S4). As before, this process can be repeated at input and output in both correction bases, while again reducing the size of the isoplanatic patches (Table. I). The final corrected FR matrix $\mathbf{R}_{xx}^{(c)}(z)$ is displayed in Fig. 1(f). Comparing this result with the initial $\overline{\mathbf{R}}_{xx}(z)$ [Fig. 1(b)] illustrates the benefit of UMI. Whereas the single scattering contribution originally spread over multiple resolution cells, it now lies along the diagonal of the FR matrix. The part of the back-scattered energy that remains off-diagonal is mainly due to multiple scattering events taking place ahead of the focal plane [9, 12]. The corresponding CMP intensity profile is shown in Fig. 1(f). A comparison with the initial profile illustrates both the gain in terms of contrast (3 dB) and resolution ($F \sim 0.9$) provided by UMI (see Table. II).

III. RESULTS

A. Ultrasound matrix image

A corrected ultrasound image $\mathcal{I}_M$ can be built from the diagonal of the corrected FR matrices $R_{xx}^{(c)}$: $\mathcal{I}_M(\mathbf{r}) = |R^{(c)}(\mathbf{r},\mathbf{r})|^2$. Fig. 2 compares the resulting image $\mathcal{I}_M$ of the human calf [Fig. 2(b)] with the original one [Fig. 2(a)]. The two images are normalized by their mean intensity and are displayed over the same dynamic range. A significant improvement of the image quality is observed. Figs. 2(c,d) display close-ups of parts of the ultrasound image (the white rectangles in Fig. 2(a,b), respectively); UMI reveals some structures that were completely blurred on the original image. In particular, muscle fibers are more easily seen. Because the probe was positioned perpendicularly to the muscle fibers, they appear as strong, point-like scatterers in the ultrasound image. With UMI, resolution is significantly improved such that fibers which were hidden in the original image are revealed, and fibers which were already visible are now significantly brighter (left part of the image, around the vein located at $[x, z] = [-3, 32]$ mm). The boundaries between each type of soft tissue also appear more continuous with UMI.

To validate those qualitative observations, the focusing criterion F has been estimated before and after the UMI process [12]. The corresponding $F-$maps are shown in Figs. 2(e,f). Most of the aberrations have been corrected by UMI and the focusing parameter F is now close to 1 over a large part of the image [Fig. 2(f)]. However, according to this criterion, the aberration correction process failed in the two gray areas of the image. The first one is located at the bottom left part of the image and corresponds to the fibula (bone). Echoes coming from this area are mainly associated with multiple scattering paths, an effect that is not tackled in this article. On the top right part of the image, the focusing criterion reveals

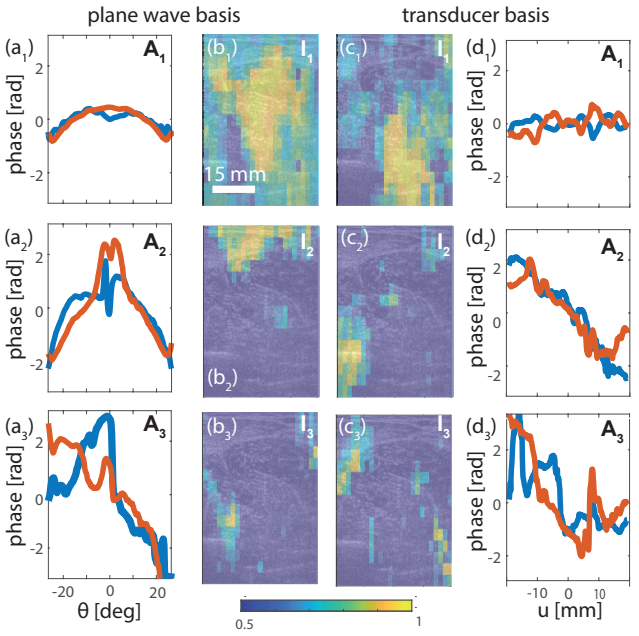

FIG. 4. Singular value distribution of the aberration matrices $\tilde{\mathbf{H}}_{\text{in}}$ and $\tilde{\mathbf{H}}_{\text{out}}$ in the plane wave and transducer bases. (a) Phase of the first three singular vectors $\mathbf{A}_p$ (from top to bottom) in the plane wave basis (blue line: $\mathbf{A}_{\text{in}}$, red line: $\mathbf{A}_{\text{out}}$) and (b) corresponding isoplanatic patches $\mathbf{I}_p$. (c) Phase of the first three singular vectors $\mathbf{A}_p$ (from top to bottom) in the transducer basis (blue line: $\mathbf{A}_{\text{in}}$, red line: $\mathbf{A}_{\text{out}}$) and (d) corresponding isoplanatic patches $\mathbf{I}_p$.

a circular area that is not well reconstructed. Two reasons could explain this result. First, plane wave imaging supposed that the medium is not moving during the entire acquisition process. Here, the ultrasound sequence is quite long (101 firings at 1000 Hz) and the existence of a vein at shallow depth could disrupt this hypothesis. Secondly, the SNR associated with this area is quite low. It thus makes the estimation of the aberration law more difficult. Nevertheless, note that, compared to the original ultrasound image, the focusing criterion can now be at least estimated in this area which means that some aberrations have been corrected. To be more quantitative, the gains in resolution and contrast are reported in Table. II for the area $\mathcal{A}_1$ depicted in Fig. 2(a). The resolution and the $F-$parameter are improved by almost a factor of 3, and the contrast (related to the single-to-multiple scattering ratio) is increased by 3 dB. This excellent performance illustrates the benefit that UMI could provide for an optimal ultrasound diagnosis.

B. Aberration matrices and isoplanatic patches

Matrix imaging also enables the mapping of aberration phase laws across the field-of-view (see Supplementary Fig. S4). Just as before, a SVD is highly useful in extracting the characteristic spatial variations of aberration. Performing this decomposition on the estimated aberration matrices $[\tilde{\mathbf{H}}_{\text{in}}, \tilde{\mathbf{H}}_{\text{out}}]$ enables the extraction of a set of isoplanatic patches for both the plane-wave and transducer bases. This can be written:

$$\left[\tilde{\mathbf{H}}_{\text{in}}, \tilde{\mathbf{H}}_{\text{out}}\right] = \sum_p s_p \mathbf{A}_p \times \mathbf{I}_p^{\dagger}. \tag{22}$$

A one-to-one association is expected between the eigenstates of the aberration matrices and the isoplanatic patches supported by the field-of-view. In fact, the latter correspond directly to the singular vectors $\mathbf{I}_p$ defined in the focused basis. The corresponding aberration phase laws, $\mathbf{A}_{\text{in},p}$ and $\mathbf{A}_{\text{out},p}$, defined either in the plane wave or transducer bases are stored in the corresponding singular vector, $\mathbf{A}_p = [\mathbf{A}_{\text{in},p}, \mathbf{A}_{\text{out},p}]$. The associated singular value s_p accounts for the degree of correlation of the extracted aberration phase laws over the field-of-view. Similarly to the distortion matrix for a specular object [13], an effective number of isoplanatic patches can be estimated from the entropy $\mathcal{H}(s_p)$ of the normalized singular values $\hat{s}_p = s_p / \sum_i s_i$: $\mathcal{H}(\hat{s}_p) = -\sum_i \hat{s}_i \log_2(\hat{s}_i)$. Here, the entropy is 6.5 and 7.0 in the Fourier and transducer bases, respectively.

Fig. 4 shows the three first eigenstates of $[\tilde{\mathbf{H}}_{\text{in}}, \tilde{\mathbf{H}}_{\text{out}}]$ in the plane wave and transducer bases. We first remark that the retrieved aberration phase laws, $\mathbf{A}_{\text{in},p}$ and $\mathbf{A}_{\text{out},p}$, are not strictly equal at input and output; this is despite the fact that the transmit and back-scattered waves travel through the same heterogeneities, and so the manifestation of aberrations should be identical in input and output. The partial non-reciprocity stems from the different input and output bases used to: (*i*) originally record the reflection matrix; (*ii*) correct aberrations at each step of the UMI process [see Table. I]. For this latter reason, some distorted components can emerge more clearly in one basis rather than the other, as aberrations in each basis are not fully independent (especially in the far-field).

Interestingly, the measured features of an isoplanatic patch differ according to the correction basis. In particular, the first two eigenstates [Figs. 4(b_1,b_2,c_1,c_2)] confirm the fact that the plane wave and transducer bases are more effective at small and large depths, respectively [Fig. 3]. Moreover, each correction basis addresses aberrations of a different nature. Indeed, the spatial extension of the isoplanatic patches is deeply affected by the correction basis, thereby impacting the result of the aberration correction process. Depending on the location of the aberrating layer and/or its spatial dimension, one basis will therefore be more suitable than another to extract the aberration law. On one hand, a local perturbation of the medium speed-of-sound located at shallow depth such as superficial veins will have a strong impact on the signals that are measured by transducers located directly above. The transducer basis is then the most adequate for those local variations of the speed-of-sound. On the other hand, in most *in-vivo* applications, the or-

gans under study are generally separated from the probe by layers of skin, adipose and/or muscle tissues. In such layered media, aberrations are invariant by translation from the plane wave basis. The first eigenstate displayed at the top of Fig. 4 confirms this statement. In the plane wave basis, the aberration phase law A_1 exhibits a concave parabolic shape characteristic of a layered medium with an under-estimated integrated speed-of-sound [14] [Fig. 4(a_1)]. In the transducer basis, it exhibits fluctuations of higher spatial frequencies characteristic of those which would be induced by local speed-of-sound variations at shallow depths [Fig. 4(d_1)].

For higher-order eigenstates, the size of the isoplanatic patches $\mathbf{I}_p$ decreases with eigenstate rank p [Figs. 4(b_2,b_3,c_2,c_3)], while the complexity of the associated aberration phase laws $\mathbf{A}_p$ increases [Figs. 4(a_2,a_3,d_2,d_3)]. Each singular vector $\mathbf{I}_p$ maps onto disjoint isoplanatic areas in the field-of-view. Interestingly, a correlation can be observed between the revealed isoplanatic patches and the tissue architecture revealed by UMI [Fig. 2(b)]. For instance, $\mathbf{I}_2$ focuses on the superficial layers of skin, fat and muscle in the plane wave basis [Fig. 4(b_2)], while in the transducer basis, it focuses on the fibula area (bottom left of the ultrasound image) [Fig. 4(c_2)]. The third-order eigenstates focus on smaller patches [5 mm, see Figs. 4(b_3,c_3)] associated with more complex aberration phase laws [Figs. 4(a_3,d_3)]. The SVD of the aberration matrices thus provides a segmentation of ultrasound images that coincides with the actual distribution of tissues in the field-of-view. This information can be useful for the quantitative mapping of relevant bio-markers such as the speed-of-sound [9, 19, 20].

IV. DISCUSSION AND PERSPECTIVES

The results presented in this paper validate the UMI process for local aberration correction in *in vivo* ultrasound imaging of the human body. Here, UMI is demonstrated on a human calf – a medium which is representative of *in-vivo* ultrasound imaging with various types of tissues and a strongly heterogeneous distribution of the speed-of-sound. The medium includes areas of both strong and weak scattering, which is a challenging problem for standard adaptive focusing techniques. The backscattered echoes are generated either by unresolved scatterers (ultrasound speckle), bright point-like scatterers (muscle fibers) or specular structures that are larger than the image resolution (for example, the skin-muscle at around $z = 5$ mm). Previous works have shown that the distortion matrix concept can be applied to both specular objects [13], random scattering media [14], or sparse media made of a few isolated scatterers [15]. The present article details a global strategy for aberration correction that is essential for applying UMI to *in-vivo* configurations where all of these scattering regimes can be found.

While our method is inspired by previous works in ultrasound imaging [6, 8, 21–23], it features several distinct and important differences. The first one is its primary building block: The broadband FR matrix that precisely selects all of the singly-scattered echoes originating from each focal point. This is a decisive step since it greatly reduces the detrimental contribution of out-of-focus and multiply-scattered echoes. Secondly, the matrix approach provides a generalization of the virtual transducer interpretation [8]. By decoupling the location of the input and output focal spots, this approach becomes flexible enough to identify and correct for aberrations at both input and output and in any correction basis, in contrast with previous works [4–6, 8]. Matrix imaging can thus easily be applied to focused excitations, diverging waves, or to other geometries like curved probes or phased arrays.

The distortion matrix constitutes a powerful tool for imaging a heterogeneous medium when little to no previous knowledge on the spatial variations of the speed-of-sound is available. An optimized contrast and a close-to-ideal resolution can be recovered for any pixel of the ultrasound image. This approach also paves the way towards a mapping of the speed-of-sound distribution inside the medium [9, 19, 20] by revealing the different isoplanatic patches in the ultrasound image. Such an optimized focusing process is also critical for accurate characterization measurements such as local measurements of ultrasound attenuation [24], scattering anisotropy [25] or the micro-architecture of soft tissues [26].

ACKNOWLEDGMENT

The authors wish to thank Victor Barolle, Amaury Badon and Thibaud Blondel whose own research works in optics and seismology inspired this study. his project has received funding from the European Research Council (ERC) under the European Union's Horizon 2020 research and innovation programme (grant agreement No. 819261); the Labex WIFI (Laboratory of Excellence within the French Program Investments for the Future, ANR-10-LABX-24 and ANR-10-IDEX-0001-02 PSL*). W.L. acknowledges financial support from the Supersonic Imagine company. L.C. acknowledges financial support from the European Union's Horizon 2020 research and innovation programme under the Marie Sklodowska-Curie grant agreement No. 744840.

Supplementary Information

This document provides further information on the retrieval of the aberration matrices $\tilde{\mathbf{H}}$ from the distortion matrices $\mathbf{D}$: (i) a workflow that sums up all the steps of the UMI procedure; (ii) a theoretical prediction of the SVD of $\mathbf{D}$ by investigating the correlation matrix $\mathbf{C} = \mathbf{D}\mathbf{D}^\dagger$; (iii) a time reversal picture of the SVD process; (iv) a potential linear phase ramp artifact on the aberration phase law and how to correct for it; (v) a description of the final steps of UMI that rely on the SVD of the normalized correlation matrix $\delta\hat{\mathbf{C}}$; (vi) an analysis of the extracted aberration phase laws in the transducer and plane wave bases.

S1. WORKFLOW

Fig. S1 shows a workflow that sums up the first two steps of the UMI procedure performed in the accompanying paper. The last two steps are equivalent but the SVD of $\mathbf{D}$ is replaced by the SVD of the normalized correlation matrix $\delta\hat{\mathbf{C}}$ to extract the residual aberration phase law $\delta\mathbf{U}_1$ (see Section. S4).

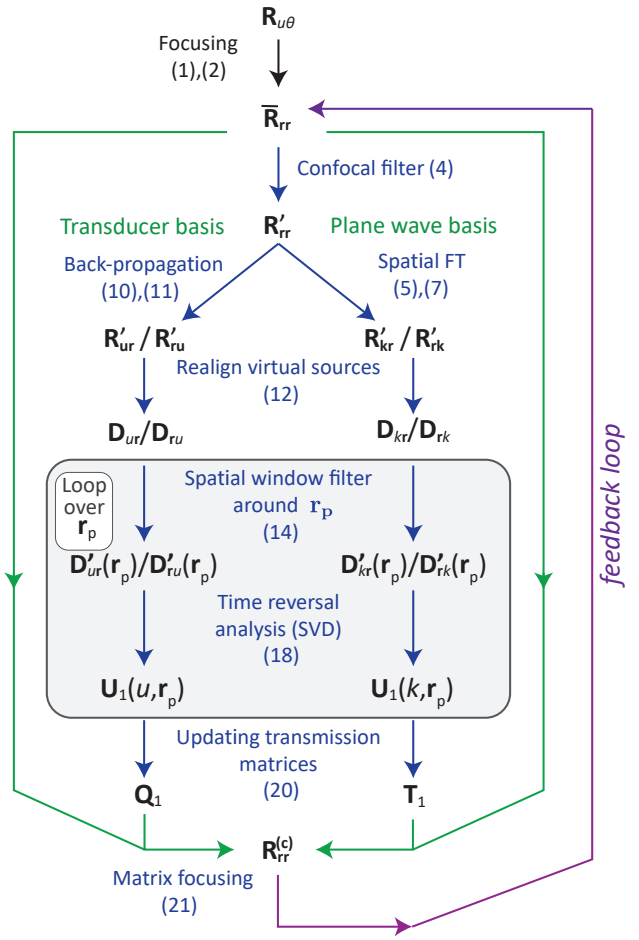

FIG. S1. Workflow of the first two steps of the aberration correction process. The blue lines refer to the estimation process of the aberration phase laws while the green lines refer to the aberration correction procedure. The purple line depicts the iteration of the UMI process. The gray rectangle symbolizes a loop over the spatial window centered on $\mathbf{r}_\mathrm{p}$.

S2. CORRELATION MATRIX

To study the SVD of the distortion matrix $\mathbf{D}'_{ur}(\mathbf{r}_\mathrm{p})$ in the transducer basis, the correlation matrix $\mathbf{C}_{uu}(\mathbf{r}_\mathrm{p})$ is needed:

$$\mathbf{C}_{uu}(\mathbf{r}_\mathrm{p}) = N_\mathrm{in}^{-1}\mathbf{D}'_{ur}(\mathbf{r}_\mathrm{p}) \times \mathbf{D}'^{\dagger}_{ur}(\mathbf{r}_\mathrm{p}), \tag{S1}$$

with N_in the number of virtual sources contained in each spatial window $\Delta\mathbf{r}$. The SVD of $\mathbf{D}'(\mathbf{r}_\mathrm{p})$ is indeed equivalent to the eigenvalue decomposition of $\mathbf{C}_{uu}(\mathbf{r}_\mathrm{p})$:

$$\mathbf{C}_{uu}(\mathbf{r}_\mathrm{p}) = \mathbf{U}(\mathbf{r}_\mathrm{p}) \times \mathbf{\Sigma}^2(\mathbf{r}_\mathrm{p}) \times \mathbf{U}^\dagger(\mathbf{r}_\mathrm{p}). \tag{S2}$$

or, in terms of matrix coefficients,

$$\mathbf{C}_{uu}(\mathbf{r}_\mathrm{p}) = \sum_i \sigma_i^2(\mathbf{r}_\mathrm{p}) U_i(u_\mathrm{out}, \mathbf{r}_\mathrm{p}) U_i^*(u_\mathrm{out}, \mathbf{r}_\mathrm{p}). \tag{S3}$$

The eigenvalues σ_i^2 of $\mathbf{C}_{uu}(\mathbf{r}_\mathrm{p})$ are the square of the singular values of $\mathbf{D}'_{ur}(\mathbf{r}_\mathrm{p})$. The eigenvectors $\mathbf{U}_i(\mathbf{r}_\mathrm{p})$ of $\mathbf{C}_{uu}(\mathbf{r}_\mathrm{p})$ are the output singular vectors of $\mathbf{D}'_{ur}(\mathbf{r}_\mathrm{p})$. The study of $\mathbf{C}_{uu}(\mathbf{r}_\mathrm{p})$ should thus lead to the prediction of the singular vectors $\mathbf{U}_i(\mathbf{r}_\mathrm{p})$.

The coefficients of $\mathbf{C}_{uu}$ can be seen as an average over $\mathbf{r}_\mathrm{in}$ of the spatial correlation of each distorted wave-field:

$$C(u, u', \mathbf{r}_\mathrm{p}) = \frac{1}{N_\mathrm{in}} \sum_{\mathbf{r}_\mathrm{in}} D'(u, \mathbf{r}_\mathrm{in}, \mathbf{r}_\mathrm{p})\ D'^*(u', \mathbf{r}_\mathrm{in}, \mathbf{r}_\mathrm{p}). \tag{S4}$$

$\mathbf{C}_{uu}$ can be decomposed as the sum of a covariance matrix $\langle\mathbf{C}_{uu}\rangle$ and a perturbation term $\mathbf{N}$:

$$\mathbf{C}_{uu} = \langle\mathbf{C}_{uu}\rangle + \mathbf{N}. \tag{S5}$$

$\mathbf{C}_{uu}$ will converge towards $\langle\mathbf{C}_{uu}\rangle$ if the perturbation term $\mathbf{N}$ tends towards zero. In fact, the intensity of $\mathbf{N}$ scales as the inverse of the number N_in of resolution cells in each sub-region [8, 27]. In the following, we will thus assume a convergence of $\mathbf{C}$ towards its covariance matrix $\langle\mathbf{C}\rangle$ due to disorder self-averaging.

The covariance matrix can be derived analytically in the speckle regime for which the medium reflectivity $\gamma(\mathbf{r})$ is assumed to be random, meaning that $\langle\gamma(\mathbf{r})\gamma^*(\mathbf{r}')\rangle = \langle|\gamma|^2\rangle\delta(\mathbf{r}-\mathbf{r}')$. Under this assumption, injecting (13) into

(S4) leads to:

$$C(u_{\rm out},u'_{\rm out},\mathbf{r}_{\rm p}) \propto \langle|\gamma|^2\rangle \tilde{H}_{\rm out}(u_{\rm out},\mathbf{r}_{\rm p})\tilde{H}^*_{\rm out}(u'_{\rm out},\mathbf{r}_{\rm p}) \left[\tilde{H}_{\rm in}{*}\tilde{H}_{\rm in}\right](u_{\rm out}-u'_{\rm out},\mathbf{r}_{\rm p}), \quad \text{(S6)}$$

where the symbol $*$ stands for a correlation product. The correlation term, $\tilde{H}_{\rm in}{*}\tilde{H}_{\rm in}$, results from the Fourier transform of the input PSF intensity $|H_{\rm in}|^2$. Equation (S6) is reminiscent of the Van Cittert-Zernike theorem for an aberrating layer [28]. This theorem states that the spatial correlation of a random wavefield generated by an incoherent source is equal to the Fourier transform of the intensity distribution of this source (here the input aberrated focal spots).

By confronting (S6) with (S3), one can show that the eigenvectors $\mathbf{U}_p$ of the correlation matrix $\mathbf{C}_{uu}$ will be proportional to the aberration transmittance $\tilde{H}_{\rm out}(u_{\rm out},\mathbf{r}_{\rm p})$. However, their amplitude is also modulated by the eigenvectors $\mathbf{W}_i$ of the correlation kernel, $\tilde{\mathbf{H}}_{\rm in}{*}\tilde{\mathbf{H}}_{\rm in} = \left[\tilde{H}_{\rm in}{*}\tilde{H}_{\rm in}\,(u_{\rm out}-u'_{\rm out})\right]$, such that

$$\mathbf{U}_i(\mathbf{r}_{\rm p}) \propto \tilde{\mathbf{H}}_{\rm out}(\mathbf{r}_{\rm p}) \circ \mathbf{W}_i(\mathbf{r}_{\rm p}). \quad \text{(S7)}$$

The eigenvectors $\mathbf{W}_i$ can be derived by solving a second order Fredholm equation with Hermitian kernel [29, 30]. An analytical solution can be found for certain analytical form of the correlation function $\tilde{H}_{\rm in}{*}\tilde{H}_{\rm in}$. In absence of aberration [$\tilde{H}_{\rm in}(u_{\rm in})=1$], the correlation function $\tilde{H}_{\rm in}{*}\tilde{H}_{\rm in}$ should be equal to a triangle function that spreads over the whole correlation matrix [8]. In presence of aberrations, a significant drop of the correlation width δu_{in} of $\tilde{H}_{\rm in}{*}\tilde{H}_{\rm in}$ is expected. δu_{in} is actually inversely proportional to the spatial extent $\overline{\delta x}_{\rm in}$ of the input PSF $H_{\rm in}$: $\delta u_{in} \sim \lambda z/\overline{\delta x}_{\rm in}$ [22]. Fig. S2(a) illustrates that fact by showing the modulus of the correlation matrix $\mathbf{C}_{uu}(\mathbf{r}_{\rm p})$ computed over the area $\mathcal{A}_2$ in Fig. S4(h). If we assume that the aberrations only induce phase retardation effects ($|\tilde{H}_{\rm out}(u_{\rm out},\mathbf{r}_{\rm p})|=1$), the modulus of $\mathbf{C}_{uu}$ is actually a direct estimator of $\tilde{\mathbf{H}}_{\rm in}{*}\tilde{\mathbf{H}}_{\rm in}$. As shown by Fig. S2(a), the correlation function $\tilde{H}_{\rm in}{*}\tilde{H}_{\rm in}$ is far from having a triangular shape and it decreases rapidly with the distance $|u_{\rm out}-u'_{\rm out}|$.

For such a bounded correlation function, the effective rank of $\mathbf{C}_{uu}$ is shown to scale as the number of resolution cells contained in the input PSF $H_{\rm in}$ [29]:

$$M_\delta \sim (\Delta u/\delta u_{\rm in}) \sim (\delta x_{\rm in}/\delta x_0) \quad \text{(S8)}$$

The shape of the corresponding eigenvectors $\mathbf{W}_i(\mathbf{r}_{\rm p})$ depends on the exact form of the correlation function. For instance, a sinc correlation function imply 3D prolate spheroidal eigenfunctions[29]; a Gaussian covariance function leads to Hermite-Gaussian eigenmodes[31]. As the correlation function $\tilde{H}_{\rm in}{*}\tilde{H}_{\rm in}$ is, in first approximation, real and positive, a general trend is that the first eigenvector $\mathbf{W}_1(\mathbf{r}_{\rm p})$ shows a nearly constant phase. This

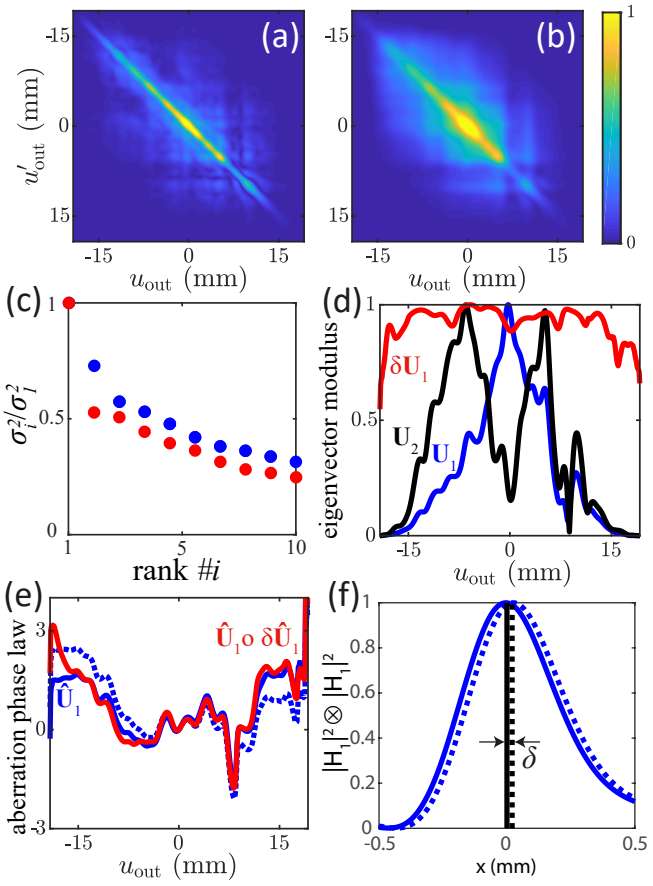

FIG. S2. Extraction of the aberration phase law from the correlation matrices in the output transducer basis computed over the area $\mathcal{A}_2$ in Fig. S4(h). (a,b) Modulus of $\mathbf{C}_{uu}$ and $\delta\mathbf{C}_{uu}$, respectively. (c) Ten first normalized eigenvalues of the correlation matrices $\mathbf{C}_{uu}$ (blue dots) and $\delta\hat{\mathbf{C}}_{uu}$ (red dots). (d) The modulus of the two first eigenvectors of $\mathbf{C}_{uu}$, $\mathbf{U}_1$ (blue line) and $\mathbf{U}_2$ (black line), is compared to the modulus of the first eigenvector $\delta\mathbf{U}_1$ of $\hat{\mathbf{C}}_{uu}$ (red line). (e) The aberration phase law $\hat{\mathbf{U}}_1$, before (dashed blue line) and after the linear phase ramp correction (continuous blue line), is compared to the final aberration phase law resulting from the combination between $\hat{\mathbf{U}}_1$ and $\delta\hat{\mathbf{U}}_1$. (f) Projection in the focal plane of the aberration phase law $\hat{\mathbf{U}}_1$ before (dashed blue line) and after the linear phase ramp correction (continuous blue line).

is a very important property since it means that the phase of the first eigenvector $\mathbf{U}_1(\mathbf{r}_{\rm p})$ is a direct estimator of $\tilde{\mathbf{H}}_{\rm out}(\mathbf{r}_{\rm p})$ [blue dashed line in Fig. S2(e)]. The modulus of $\mathbf{U}_1(\mathbf{r}_{\rm p})$, *i.e* $\mathbf{W}_1(\mathbf{r}_{\rm p})$, generally exhibits a single lobe around $u_{\rm out}=0$. Its typical width is the correlation length $\delta u_{\rm in}$. The higher rank eigenvectors $\mathbf{W}_i(\mathbf{r}_{\rm p})$ are more complex and exhibit a number of lobes that scales with their rank i. The blue and black lines in Fig. S2(d) show the modulus of the first two eigenvectors of the matrix $\mathbf{C}_{uu}$ displayed in Fig. S2(a). We recognize the typical signature of the two first eigenmodes with one and two lobes respectively.

To sum up, the phase of the first singular vector $\mathbf{U}_1$ of the output distortion matrix $\mathbf{D}'_{ur}(\mathbf{r}_\mathrm{p})$ is an estimator of the output aberration phase law. However, this estimation is degraded by the aberrations in transmit. The support of $\mathbf{U}_1$ actually scales as the correlation width δu_in of aberrations in the transducer basis. For aberration correction, it is thus important to consider the normalized vector $\hat{\mathbf{U}}_1 = [U_1(u_\mathrm{out})/|U_1(u_\mathrm{out})]$ that only implies a phase shift and not the full amplitude of $\mathbf{U}_1$ as it is, however, done in Ref. [4]. In the latter case, the bounded support of $\mathbf{U}_1$ would limit the probe aperture to the correlation width δu_in. For a strong level of aberrations, it can deeply degrade the resolution of the corrected image. Nevertheless, it should kept in mind that the estimation of the aberration phase law by $\hat{\mathbf{U}}_1$ is altered on the edges of the array. The theoretical prediction of (S7) remains actually valid if the noise variance $\left\langle |N(u_\mathrm{out}, u'_\mathrm{out})|^2 \right\rangle$ in (S5) is smaller than the signal intensity $|\langle C(u_\mathrm{out}, u'_\mathrm{out})\rangle|^2$. As $\left\langle |N(u_\mathrm{out}, u'_\mathrm{out})|^2 \right\rangle = \left\langle |C(u_\mathrm{out}, u_\mathrm{out})|^2 \right\rangle / N_\mathrm{in}$, it yields the following condition:

$$N_\mathrm{in} > \eta_\mathrm{in}(u_\mathrm{out} - u'_\mathrm{out}) \tag{S9}$$

with $\eta_\mathrm{in} = [\tilde{H}_\mathrm{in} * \tilde{H}_\mathrm{in}](u_\mathrm{out} - u'_\mathrm{out}) / \left|\tilde{H}_\mathrm{in}(u_\mathrm{out})\right|^2$, the normalized autocorrelation of the input aberration transmittance $\tilde{H}_\mathrm{in}$. For a Gaussian covariance function, such that $\eta_\mathrm{in}(\delta u) = \exp\left[-\delta u^2/(2\delta u_\mathrm{in}^2)\right]$, the effective aperture δu_c of $\hat{\mathbf{U}}_1$, i.e the distance range of transducers over which $\hat{\mathbf{U}}_1$ is a correct estimator of $\tilde{\mathbf{H}}_\mathrm{out}(\mathbf{r}_\mathrm{p})$, can be deduced

$$\delta u_c \sim \Delta u \frac{\sqrt{\ln(N_\mathrm{in})}}{M_\delta} \tag{S10}$$

In other words, a correct estimation of the aberration phase law over the whole numerical aperture ($\delta u_c \sim \Delta u$) is obtained provided that :

$$N_\mathrm{in} \sim \exp(M_\delta^2). \tag{S11}$$

S3. TIME REVERSAL PICTURE AND POTENTIAL ARTIFACT

A time reversal picture for the SVD process is provided to interpret physically the different theoretical elements described in the previous paragraph. This picture will also show how a potential artifact may arise in the estimated aberration phase law and how to correct for it.

The previous paragraph has shown that the aberration phase law can be extracted from the SVD of the distortion matrix $\mathbf{D}'_{ur}(\mathbf{r}_\mathrm{p})$. This operation can be actually seen as a fictive time reversal experiment. Expressed in the form of Eq. S6, $\mathbf{C}_{uu}$ is analogous to a reflection matrix $\mathbf{R}$ associated with a single scatterer of reflectivity $|H_\mathrm{in}(x)|^2$ [Fig. S3(c)]. For such an experimental configuration, it has been shown that an iterative time reversal process converges towards a wavefront that focuses perfectly through the heterogeneous medium onto this scatterer [32, 33]. Interestingly, this time-reversal invariant can also be deduced from the eigenvalue decomposition of the time-reversal operator $\mathbf{R}\mathbf{R}^\dagger$ [32–34]. The same decomposition could thus be applied to $\mathbf{C}_{uu}$ in order to retrieve the wavefront that would perfectly compensate for aberrations and optimally focus on the virtual reflector. This effect is illustrated in Fig. S3(c). It is important to emphasize, however, that the coherent reflector is enlarged compared to the diffraction limit. As seen before (S7), a set of eigenmodes $\mathbf{U}_i$ are thus obtained and focus on different parts of the virtual reflector [29, 31]. Generally, the first eigenvector $\mathbf{U}_1$ focuses on the center of the virtual reflector since it maximizes the back-scattered energy. Its phase thus directly maps onto the aberration transmittance.

However, it might not be the case if the scattering distribution $|H_\mathrm{in}(x)|^2$ is too complex. $\mathbf{U}_1$ then focuses on the brightest spot exhibited by the input PSF $|H_\mathrm{in}(x)|^2$. The phase of $\mathbf{U}_1$ can then exhibit an additional linear phase ramp compared to the *true* aberration phase law [23]:

$$\hat{U}_1(u_\mathrm{out}) = \tilde{H}_\mathrm{out}(u_\mathrm{out}) e^{-i\frac{k_c}{2z}u_\mathrm{out}x_0} \tag{S12}$$

where x_0 corresponds to the lateral shift of the corresponding PSF H_1, such that

$$H_1(x) = \sum_{u_\mathrm{out}} \hat{U}_1(u_\mathrm{out}) e^{i\frac{k_c}{2z}u_\mathrm{out}x} = H_1(x - x_0). \tag{S13}$$

If no effort is made to remove this shift, each selected area defined by the spatial window function (14) could suffer from arbitrary lateral shifts x_0 compared to the original image. This artifact can be suppressed by removing the linear phase ramp in (S12). One way to do it consists in estimating the corresponding shift x_0 by considering the auto-convolution product of the incoherent PSF $|H_1|^2$:

$$\left[|H_1|^2 \overset{x}{\circledast} |H_1|^2\right](x) = \left[|H_\mathrm{out}|^2 \overset{x}{\circledast} |H_\mathrm{out}|^2\right](x - 2x_0) \tag{S14}$$

If a Gaussian covariance model is assumed for aberrations, the auto-convolution $|H_\mathrm{out}|^2 \overset{x}{\circledast} |H_\mathrm{out}|^2$ should be maximum at $x = 0$. In that case, the maximum position of $|H_1|^2 \overset{x}{\circledast} |H_1|^2(x)$ leads to an estimation of $2x_0$. Fig. S2(f) displays the function $\left[|H_1|^2 \overset{x}{\circledast} |H_1|^2\right](x)$ for the aberration phase law $\hat{\mathbf{U}}_1$ displayed in Fig. S2(e). Its shift with respect to the origin yields an estimation of the lateral shift x_0. Once the latter parameter is known, the undesired linear ramp can be removed from $\hat{\mathbf{U}}_1$ (S12), as illustrated in Fig. S2(e).

In the present case, this linear phase ramp compensation is applied to each estimated aberration phase law. Nevertheless, it should be noted that an aberrating layer

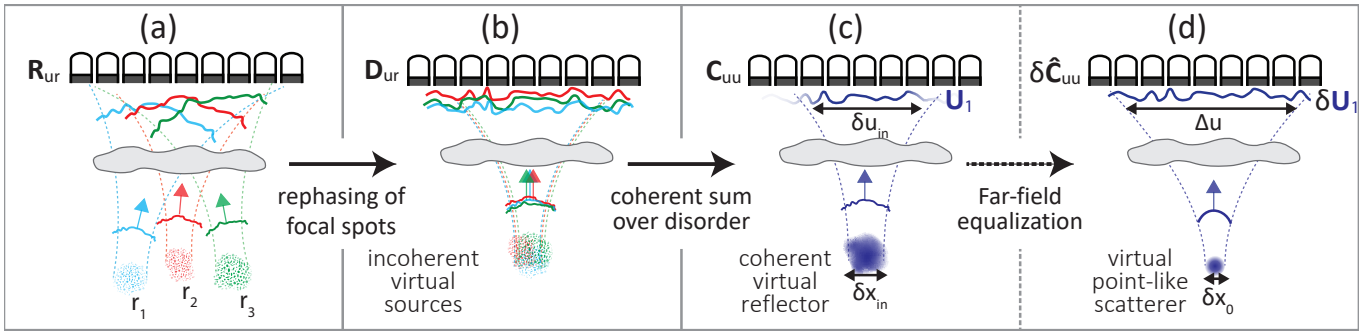

FIG. S3. Sketch of the time reversal analysis of the distortion matrix. (a) Each column of the reflection matrix $\mathbf{R}_{ur}$ corresponds to the reflected wavefield induced by the associated virtual source $\mathbf{r_{in}}$. (b) By removing the geometrical curvature of each reflected wavefront (12), the resulting distortion matrix extracts the aberrated component of those wavefronts. From an other point of view, all the wavefronts are realigned as if they were generated by input focal spots that are virtually shifted at the origin (13). (C) The correlation matrix $\mathbf{C}_{uu}$ of $\mathbf{D}_{ur}$ mimics the time reversal operator applied to a virtual reflector that results from a coherent average of all the shifted input focal spots. The phase conjugate of its first eigenvector $\mathbf{U}_1$ then yields the phase law to focus on this coherent reflector. (d) The normalized correlation matrix $\delta\hat{\mathbf{C}}_{uu}$ makes the virtual reflector point-like. The associated eigenvector $\delta\mathbf{U}_1$ yields a more accurate estimator of the aberration phase law, especially on the edges of the array.

with a particular shape such as wedges can manifest itself as a linear phase ramp in the aberration phase law. For such a particular case, the lateral shift observed on the corresponding PSF is physical and should not be compensated. The removal of the linear phase ramp should thus be used with caution as it could cancel, in some specific cases, the benefits of the aberration correction process.

S4. NORMALIZED CORRELATION MATRIX

To accelerate the convergence process and compensate for the residual aberrations more efficiently, an alternative is to normalize the correlation matrix in order to make the virtual scatterer point-like [14] [see Fig. S3(d)].

It first consists in building a residual distortion matrix $\delta\mathbf{D}_{ur}$ from the updated focused reflection matrix $\mathbf{R}_{\mathbf{rr}}^{(c)}$ obtained after the first two steps of UMI. The corresponding correlation matrix, $\delta\mathbf{C}_{uu}(\mathbf{r}_\mathrm{p}) = \delta\mathbf{D}'_{\boldsymbol{ur}}(\mathbf{r}_\mathrm{p}) \times \delta\mathbf{D}'^{\dagger}_{\boldsymbol{ur}}(\mathbf{r}_\mathrm{p})$, is then investigated. By analogy with (S6), its coefficients can be expressed as follows:

$$\delta C(u_\mathrm{out}, u'_\mathrm{out}, \mathbf{r}_\mathrm{p}) \propto \langle|\gamma|^2\rangle \delta\hat{H}_\mathrm{out}(u_\mathrm{out}, \mathbf{r}_\mathrm{p}) \delta\tilde{H}^*_\mathrm{out}(u'_\mathrm{out}, \mathbf{r}_\mathrm{p}) \left[\delta\tilde{H}_\mathrm{in} * \delta\tilde{H}_\mathrm{in}\right](u_\mathrm{out}, u'_\mathrm{out}, \mathbf{r}_\mathrm{p}), \quad \text{(S15)}$$

where $\delta\tilde{H}_\mathrm{out}$ and $\delta\tilde{H}_\mathrm{in}$ accounts for the residual aberration transmittance at output and input. As previously highlighted in Sec. S2, the correlation kernel, $\delta\tilde{\mathbf{H}}_\mathrm{in} * \delta\tilde{\mathbf{H}}_\mathrm{in}$, is a manifestation of the finite size of the virtual reflector in (S15) [Fig. S3(c)], which prevents a proper estimation of the aberration phase transmittance on the edges of the array.

Experimentally, this correlation kernel can be extracted from the modulus of $\delta\mathbf{C}_{uu}$. Fig. S2(b) shows the corresponding quantity over the area $\mathcal{A}_2$ displayed in Fig. S4(h). The comparison with the initial correlation matrix [Fig. S2(a)] already shows the drastic flattening of the correlation function $\delta\tilde{H}_\mathrm{in} * \delta\tilde{H}_\mathrm{in}$. This flattening is a direct indicator of the gain in input focusing quality provided by the first two steps of the aberration correction process. This also means that the phase of the correlation matrix can be estimated correctly even for coefficients associated with couple of transducers (u_out,u'_out) far from each other. The detrimental effect of the correlation kernel can thus be overcome by normalizing the correlation matrix as follows:

$$\delta\hat{C}(u_\mathrm{out}, u'_\mathrm{out}, \mathbf{r}_\mathrm{p}) = \frac{\delta C(u_\mathrm{out}, u'_\mathrm{out}, \mathbf{r}_\mathrm{p})}{|\delta C(u_\mathrm{out}, u'_\mathrm{out}, \mathbf{r}_\mathrm{p})|}. \quad \text{(S16)}$$

By injecting (S6) into (S16), the normalized correlation matrix coefficients $\delta\hat{C}(u_\mathrm{out}, u'_\mathrm{out}, \mathbf{r}_\mathrm{p})$ can actually be expressed as follows:

$$\delta\hat{C}(u_\mathrm{out}, u'_\mathrm{out}, \mathbf{r}_\mathrm{p}) \propto \langle|\gamma|^2\rangle \delta\tilde{H}_\mathrm{out}(u_\mathrm{out}, \mathbf{r}_\mathrm{p}) \delta\tilde{H}^*_\mathrm{out}(u'_\mathrm{out}, \mathbf{r}_\mathrm{p}) \quad \text{(S17)}$$

Expressed in this form, the normalized correlation matrix $\delta\hat{\mathbf{C}}_{uu}$ is analogous to a reflection matrix associated with a single point-like scatterer. The normalization of $\delta\mathbf{C}_{uu}$ thus equalizes the Fourier spectrum of the virtual reflector, which tends to make it point-like [Fig. S3(d)]. As in an iterative time-reversal experiment with a point-like target[32], $\delta\hat{\mathbf{C}}_{uu}$ is ideally of rank one. In practice, $\delta\hat{\mathbf{C}}_{uu}$ is still polluted by a perturbation term $\mathbf{N}$ (S5). Its rank is thus not finite but its first eigenvalue $\hat{\sigma}_1$ stands out clearly from the noise continuum, as shown by Fig. S2(c). The first eigenstate is thus associated with the virtual reflector. The associated eigenvector $\delta\mathbf{U}_1(\mathbf{r}_\mathrm{p})$ directly

yields the residual aberration phase law:

$$\delta U_1(u_{\rm out},\mathbf{r}_{\rm p}) = \delta\tilde{H}_{\rm out}(u_{\rm out},\mathbf{r}_{\rm p}) \tag{S18}$$

Fig. S2 illustrates the benefit of the normalization of δC_{uu} by considering the example of the region $\mathcal{A}_2$ in Fig. S4(h). Fig. S2(d) shows the modulus of $\delta\mathbf{U}_1$. Compared to the initial eigenvector $\mathbf{U}_1$ that shows a finite support along the transducer array, $\delta\mathbf{U}_1$ exhibits a flat amplitude which is a manifestation of a point-like virtual reflector. This implies a correct estimation of the residual aberration phase transmittance for all transducers. A novel estimator $\mathbf{Q}_2$ of the transmission matrix can be built by combining the initial and additional corrections:

$$\mathbf{Q}_2 = \mathbf{Q}_0 \circ \hat{\mathbf{U}}_1^* \circ \delta\hat{\mathbf{U}}_1^* \tag{S19}$$

Fig. S2(e) displays the accumulated phase of the aberration transmittance estimator, $\hat{\mathbf{U}}_1 \circ \delta\hat{\mathbf{U}}_1$. Compared to $\hat{\mathbf{U}}_1$, the additional correction $\delta\hat{\mathbf{U}}_1$ introduces a significant modification of the aberration phase law on the edge of the ultrasound probe. An updated FR matrix $\mathbf{R}_{xx}^{(c)}(z)$ can be finally obtained:

$$\mathbf{R}_{xx}^{(c)}(z) = \mathbf{Q}_2^{\dagger}(z) \times \mathbf{Q_0}(z) \times \overline{\mathbf{R}}_{xx}(z). \tag{S20}$$

As done in the accompaying paper, this aberration correction process can be repeated at input in the plane wave basis and then by exchanging the correction bases at input and output, while reducing again the size of isoplanatic patches (see Table.1).

Although the normalization operation in (S16) tends to make the virtual scatterer point-like and improves the estimation of the aberration phase law, this alternative time reversal process should be used with caution. Indeed, correlation coefficients associated with transducers far from each other exhibit a lower SNR [Fig. S2(b)]. The convergence of the correlation matrix towards the covariance matrix should thus be priorly ensured before employing this trick. Here, in the present case, the overall imaging process has been divided into fours steps [see Table. 1]. The time reversal analysis is applied to the distortion matrix, or equivalently to the correlation matrix $\mathbf{C}$, in the two first steps of the matrix imaging process for sake of robustness to multiple scattering noise. The weak accuracy of the aberration phase law at large angles or on the edges of the array is then addressed in the two last steps by considering the normalized correlation matrix $\delta\hat{\mathbf{C}}$.

S5. ABERRATION PHASE LAWS

Fig. S4 shows the spatial distribution of aberrations phase laws at the end of the matrix imaging process. The truncated aspect of some of the aberration laws results from the maximal angles of illumination or collection imposed by the finite size of the ultrasonic array. At small depths [$z < A\tan[\beta(\mathbf{r})]/2$, see Fig. 3(l)], the spatial extension of the reflected wave-field is limited by the numerical aperture of the probe [see e.g Fig. S4(a_2)]. A plane wave basis is thus more adequate since its angular range is almost invariant over the focal plane [see Fig. S4(a_1)]. On the contrary, in the far-field, the angular range of plane waves reaching each focal point is limited by the physical aperture of the probe [see Fig. 3(l)]. Hence the transducer basis should be favoured in that case [see e.g S4(g)].

Fig. S4 highlights the spatial variations of the aberration phase across the field-of-view. The spatial resolution of the aberration map has been made possible by gradually reducing the size of the spatial window $W_{\mathbf{\Delta r}}$ at each step of the matrix imaging process (see Table. 1). The four colored straight rectangles in Fig. 2(a) depict the size of the spatial windows used at each step. A 75% overlapping is applied between each spatial window in order to retrieve the aberration matrix $\tilde{\mathbf{H}}_{\rm in/out}$ at a high resolution $\mathbf{\Delta r}$. Some aberration laws corresponding to adjacent areas [Fig. S4(b,c,d)] are highly correlated, both in the plane wave or transducer bases, meaning that their associated rectangle areas belong to the same isoplanatic patch. On the contrary, areas separated by more than a resolution cell $\mathbf{\Delta r}$ seem to display un-correlated aberration phase laws. These spatial correlations in the aberration matrices are quantitatively investigated through the SVD of the aberration matrices in the accompanying paper (Section III.C).

[1] L. M. Hinkelman, T. L. Szabo, and R. C. Waag, J. Acoust. Soc. Am. **101**, 2365 (1997).
[2] J. J. Dahl, M. S. Soo, and G. E. Trahey, IEEE Trans. Ultrason. Ferroelectr. Freq. Control **52**, 1504 (2005).
[3] F. A. Duck, Physical properties of tissue: A comprehensive reference book , 73 (1990).
[4] H. Bendjador, T. Deffieux, and M. Tanter, IEEE Trans. Med. Imag. **39**, 3100 (2020).
[5] G. Chau, M. Jakovljevic, R. Lavarello, and J. Dahl, Ultrasonic imaging **41**, 3 (2019).
[6] G. Montaldo, M. Tanter, and M. Fink, Phys. Rev. Lett. **106**, 054301 (2011).
[7] B.-F. Osmanski, G. Montaldo, M. Tanter, and M. Fink, IEEE Trans. Ultrason. Ferroelectr. Freq. Control **59**, 1575 (2012).
[8] J.-L. Robert and M. Fink, J. Acoust. Soc. Am. **123**, 866 (2008).
[9] W. Lambert, L. A. Cobus, M. Couade, M. Fink, and A. Aubry, Phys. Rev. X **10**, 021048 (2020).
[10] T. Blondel, J. Chaput, A. Derode, M. Campillo, and A. Aubry, J. Geophys. Res.: Solid Earth **123**, 10936 (2018).
[11] A. Badon et al., Sci. Adv. **2**, e1600370 (2016).
[12] W. Lambert, L. C. Cobus, M. Fink, and A. Aubry, arXiv:

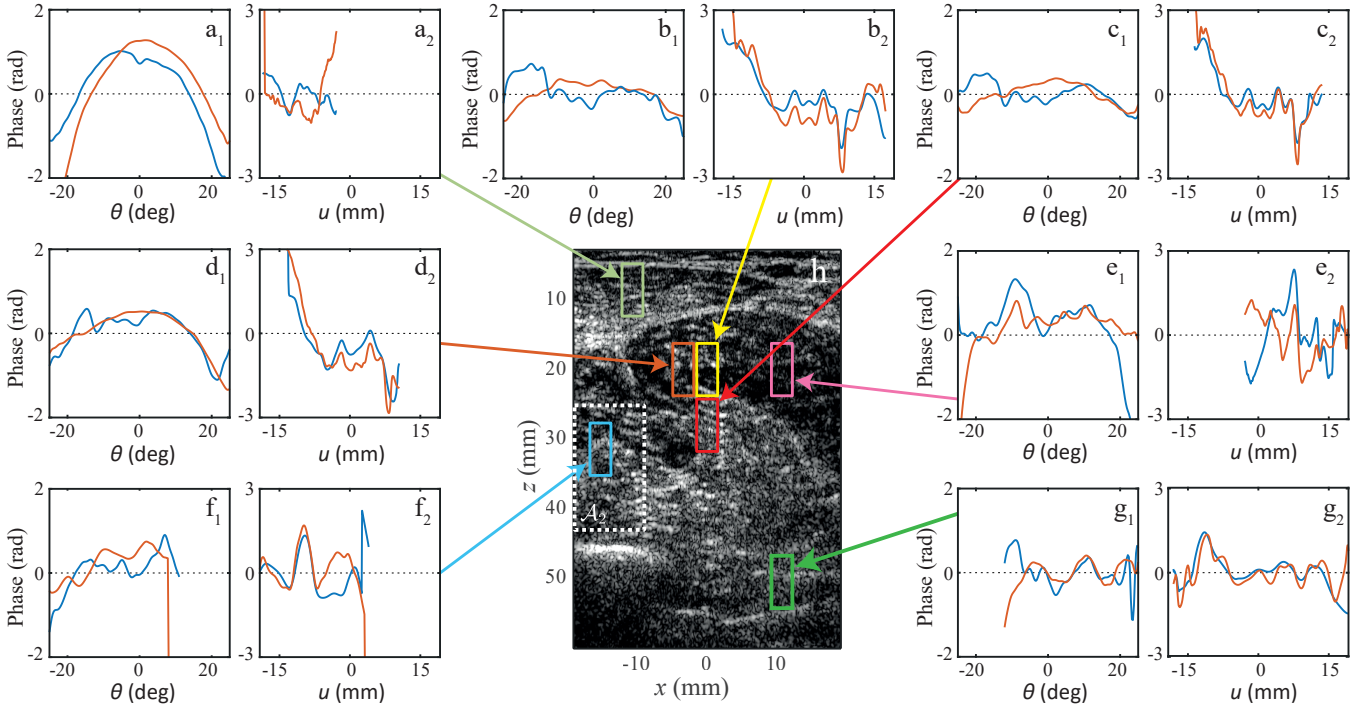

FIG. S4. Examples of aberration phase laws resulting from the matrix imaging process, computed in transmit (blue curves) and in receive (red curves) modes, in the plane wave (1) and transducer (2) bases. The dimension of the selected areas is defined by the size of the spatial window used at the fourth step of the whole process (see Table.1).

2103.02029 (2021).
[13] A. Badon et al., Sci. Adv. **6**, eaay7170 (2020).
[14] W. Lambert, L. A. Cobus, T. Frappart, M. Fink, and A. Aubry, Proc. Natl. Acad. Sci. USA **117**, 14645 (2020).
[15] R. Touma, R. Blondel, A. Derode, M. Campillo, and A. Aubry, arXiv: 2008.01608 (2020).
[16] S.-E. Måsøy, T. Varslot, and B. Angelsen, J. Acoust. Soc. Am. **117**, 450 (2005).
[17] G. Montaldo, M. Tanter, J. Bercoff, N. Benech, and M. Fink, IEEE Trans. Ultrason., Ferroelectr., Freq. Control **56**, 489 (2009).
[18] J. W. Goodman, *Introduction to Fourier Optics* (McGraw-Hill, Inc., 1996) p. 491.
[19] M. Imbault et al., Phys. Med. Biol. **62**, 3582 (2017).
[20] P. Stähli, M. Frenz, and M. Jaeger, IEEE Trans. Med. Imaging **40**, 457 (2021).
[21] M. O'Donnell and S. Flax, IEEE Trans. Ultrason., Ferroelectr., Freq. Control **35**, 768 (1988).
[22] R. Mallart and M. Fink, J. Acoust. Soc. Am. **96**, 3721 (1994).
[23] T. Varslot, H. Krogstad, E. Mo, and B. A. Angelsen, J. Acoust. Soc. Am. **115**, 3068 (2004).
[24] K. Suzuki et al., Ultrasound Med. Biol. **18**, 657 (1992).
[25] A. Rodriguez-Molares, A. Fatemi, L. Løvstakken, and H. Torp, IEEE Trans. Ultrason. Ferroelectr. Freq. Control **64**, 1285 (2017).
[26] E. Franceschini and R. Guillermin, J. Acoust. Soc. Am. **132**, 3735 (2012).
[27] J.-L. Robert, *Evaluation of Green's functions in complex media by decomposition of the Time Reversal Operator: Application to Medical Imaging and aberration correction*, Ph.D. thesis, Universite Paris 7 - Denis Diderot (2007).
[28] R. Mallart and M. Fink, J. Acoust. Soc. Am. **90**, 2718 (1991).
[29] J.-L. Robert and M. Fink, J. Acoust. Soc. Am. **125**, 218 (2009).
[30] R. G. Ghanem and P. D. Spanos, *Stochastic finite elements: a spectral approach* (Courier Corporation, 2003) Chap. 2.
[31] A. Aubry, J. de Rosny, J.-G. Minonzio, C. Prada, and M. Fink, J. Acoust. Soc. Am. **120**, 2746 (2006).
[32] C. Prada and M. Fink, Wave Motion **20**, 151 (1994).
[33] C. Prada, S. Manneville, D. Spoliansky, and M. Fink, J. Acoust. Soc. Am. **99**, 2067 (1996).
[34] C. Prada and J.-L. Thomas, J. Acoust. Soc. Am. **114**, 235 (2003).